

**An idealized model sensitivity study on Dead Sea desertification with a focus on  
the impact on convection**

Samiro Khodayar<sup>1,2</sup> and Johannes Hoerner<sup>2</sup>

<sup>1</sup>Institute of Meteorology and Climate Research (IMK-TRO), Karlsruhe Institute of  
Technology (KIT), Karlsruhe, Germany

<sup>2</sup>Mediterranean Centre for Environmental Studies (CEAM), Valencia, Spain

Submitted to Atmospheric Chemistry and Physics

(HyMeX Inter-journal SI)

\* Corresponding author. E-mail address: Khodayar\_sam@gva.es (S. Khodayar)

Mediterranean Centre for Environmental Studies (CEAM),

Technological Park, Charles R. Darwin Street, 14 46980 - Paterna - Valencia - Spain

1 **Abstract**

2 The Dead Sea desertification-threatened region is affected by continual lake level  
3 decline and occasional, but life-endangering flash-floods. Climate change has  
4 aggravated such issues in the past decades. In this study, the impact on local  
5 conditions leading to heavy precipitation of the changing conditions of the Dead Sea is  
6 investigated. Idealized sensitivity simulations with the high-resolution convection-  
7 permitting regional climate model COSMO-CLM and several numerical weather  
8 prediction (NWP) runs on an event time scale are performed over the Dead Sea area.  
9 The simulations are idealized in the sense of the Dead Sea model representation not  
10 accurately representing the real conditions, but given by an external date set. A  
11 reference or Dead Sea simulation covering the 2003 to 2013 period and a twin  
12 sensitivity or bare soil simulation, in which the Dead Sea is set to bare soil, are  
13 compared. NWP simulations focus on heavy precipitation events exhibiting relevant  
14 differences between the Dead Sea and the bare soil decadal realization to assess the  
15 impact on the underlying convection-related processes.

16 The changing in the conditions of the Dead Sea is seen to affect the atmospheric  
17 conditions leading to convection in two ways: (a) the local decrease in evaporation  
18 reduces moisture availability in the lower boundary layer locally and in the  
19 neighbouring, directly affecting atmospheric stability. Weaker updrafts characterize the  
20 drier and more stable atmosphere of the simulations where the Dead Sea has been  
21 dried out. (b) Thermally driven wind system circulations and resulting  
22 divergence/convergence fields are altered preventing in many occasions convection  
23 initiation because of the omission of convergence lines. On a decadal scale, the  
24 difference between the simulations suggests a weak decrease in evaporation, higher  
25 air temperatures and less precipitation (less than 0.5 %).

26

27

28

29

30 *Key Words: Dead Sea desertification, climate change, convection, heavy precipitation,*  
31 *boundary layer, wind systems, high-resolution modelling*

32

33        **1. Introduction**

34        The Eastern Mediterranean and the Middle East is a sensitive climate change area  
35        (Smiatek et al. 2011). The anticipated warming in the 21<sup>st</sup> century combined with the  
36        general drying tendency, suggest important regional impacts of climate change, which  
37        should be investigated to assess and mitigate local effects on society and ecosystems.  
38        The Dead Sea basin is dominated by semi-arid and arid climates except by the north-  
39        western part that is governed by Mediterranean climate (Greenbaum et al. 2006). It is  
40        an ideal area to study climate variation in the Near East. It was already discussed by  
41        Ashbel (1939) the influence of the Dead Sea on the climate of its neighbouring regions.  
42        The change in the climate of the Dead Sea basin caused by the drying of the Dead Sea  
43        has also been evidenced in the last decades (Alpert et al. 1997; Cohen and Stanhill  
44        1996; Stanhill 1994). The Dead Sea is the lowest body of water in the world (~ -430 m)  
45        surrounded by the Judean Mountains (up to ~ 1 km amsl) to the west and to the east  
46        by the Maob Mountains (up to ~ 3 km amsl). The area in between is rocky desert. The  
47        complex topography of the area favours the combined occurrence of several wind  
48        regimes in addition to the general synoptic systems, namely valley and slope winds,  
49        Mediterranean breezes and local lake breezes (e.g. Shafir and Alpert 2011). These  
50        wind systems are of great importance for the living conditions in the region since they  
51        influence the visibility and the air quality (e.g. Kalthoff et al. 2000; Corsmeier et al.  
52        2005) as well as the atmospheric temperature and humidity. Since the Dead Sea is a  
53        terminal lake of the Dead Sea Valley, no natural outflow exists; evaporation is the main  
54        loss of water. The wind velocity and vapour pressure deficit are identified as the main  
55        governing factors of evaporation throughout the year (Metzger et al. 2017). Through  
56        the high evaporation the lake level declines and results in a desertification of the  
57        shoreline and a changing fraction of water and land surface in the valley. The  
58        documented Dead Sea water level drop of about 1 m/y in the last decades (Gavrieli et  
59        al. 2005) is mainly due to the massive water consumption at its upstream having  
60        climate changes a small contribution to the lake level decrease (Lensky and Dente  
61        2015). This situation severely affects agriculture, industry and the environmental  
62        conditions in the area, thus, leading to substantial economic losses (Arkin and Gilat  
63        2000).

64        The Jordan River catchment and Dead Sea-exhibit in the north, annual precipitation in  
65        the order of 600-800 mm, whereas in the south, there is an all year arid climate with an  
66        annual precipitation of <150 mm (Schaedler and Sasse 2006). Rain occurs between  
67        October and May and can be localized or widespread (Dayan and Sharon 1980)  
68        (Sharon and Kutiel 1986). Rainfall varies seasonally and annually, and it is often

69 concentrated in intense showers (Greenbaum et al. 2006) caused mainly by severe  
70 convection (Dayan and Morin 2006). Flash floods are among the most dangerous  
71 meteorological hazards affecting the Mediterranean countries (Llasat et al 2010), thus,  
72 knowledge about the processes shaping these events is of high value. This is  
73 particularly relevant in arid climates, where rainfall is scarce, and often, local and highly  
74 variable. In flood-producing rainstorms, atmospheric processes often act in concert at  
75 several scales. Synoptic-scale processes transport and redistribute the excess sensible  
76 and latent heat accumulated over the region and subsynoptic scale processes  
77 determine initiation of severe convection and the resulting spatio-temporal rainfall  
78 characteristics. The main responsible synoptic weather patterns leading to heavy  
79 rainfall in the region are in general well known and described in previous publications  
80 (e.g. Belachsen et al. 2017; Dayan and Morin 2006). Belachsen et al. (2017) pointed  
81 out that three main synoptic patterns are associated to these heavy rain events: Cyprus  
82 low accounting for 30% of the events, Low to the east of the study region for 44%, and  
83 Active Red Sea Trough for 26%. The first two originate from the Mediterranean Sea,  
84 while the third is an extension of the Africa monsoon. Houze (2012) showed that  
85 orographic effects lead to enhanced rainfall generation; rain cells are larger where  
86 topography is higher. Sub-synoptic scale processes play a decisive role in deep  
87 convection generation in the region. Convection generated by static instability seems to  
88 play a more important role than synoptic-scale vertical motions (Dayan and Morin  
89 2006). The moisture for developing intensive convection over the Dead Sea region can  
90 be originated from the adjacent Mediterranean Sea (Alpert und Shay-EL 1994) and  
91 from distant upwind sources (Dayan and Morin 2006).

92 In this study, the sensitivity of the local conditions to the changing conditions of the  
93 Dead Sea is investigated. The relevance of the Dead Sea as a local source of moisture  
94 for precipitating convection as well as the impact of the energy balance partitioning  
95 changes and related processes caused by setting the Dead Sea to bare soil are  
96 investigated. With this purpose, an idealized sensitivity experiment with the high-  
97 resolution regional climate model COSMO-CLM [Consortium for Small scale Modelling  
98 model (COSMO)-in Climate Mode (CLM); Böhm et al. 2006] is conducted. The high  
99 horizontal grid spacing used (~ 2.8 km) resolves relevant orographic and small-scale  
100 features of the Dead Sea basin, which is not the case when coarser resolution  
101 simulations are performed. Moreover, at this resolution convection is explicitly resolved  
102 instead of being parametrized, which has been already extensively demonstrated to be  
103 highly beneficial for the simulation of heavy precipitation and convection-related  
104 processes. The benefit of employing high-resolution convection permitting simulations

105 is mainly in sub-daily time-scales, (e.g., Prein et al., 2013; Fosser et al., 2014; Ban et  
106 al., 2014), however, daily precipitation is also positively affected, particularly in winter  
107 time (Fosser et al., 2014). Previous studies in the area applying high-resolution  
108 modelling agree with the beneficial impact of finer resolution against coarser ones (e.g.  
109 Rostkier-Edelstein et al. 2014; Hochman et al. 2018; Kunin et al. 2019).

110 A decadal simulation and several event-based Numerical Weather Prediction (NWP)  
111 runs covering the eastern Mediterranean are carried out. A process understanding  
112 methodology is applied to improve our knowledge about how sub-synoptic scale  
113 processes leading to severe convection are affected. The article is organized as  
114 follows. Section 2 provides an overview of the data and the methodology used. Then,  
115 in section 3, the climatology of the region based on the high-resolution convection-  
116 permitting decadal simulation is presented and the impact of changing conditions of the  
117 Dead Sea is examined across scales. Finally, conclusions are discussed in section 4.

118

## 119 **2. Data and methodology**

### 120 **2.1 The COSMO-CLM model**

121 In this investigation, the regional climate model (RCM) of the non-hydrostatic COSMO  
122 model, COSMO-CLM (CCLM), is used (Version 5.0.1). It has been developed by the  
123 Consortium for Small-scale modeling (COSMO) and the Climate Limited-area Modeling  
124 Community (CLM) (Böhm et al., 2006). It uses a rotated geographical grid and a  
125 terrain-following vertical coordinate. The model domain covers the southern half of the  
126 Levant, centred around the Dead Sea, with a horizontal resolution of 7 km and 2.8 km,  
127 60 vertical levels and a time step of 60 and 20 seconds, respectively. Using IFS  
128 (Integrated Forecasting System) analysis, the spectral weather model of ECMWF  
129 (European Centre for Medium-Range Weather Forecast) as driving data for the  
130 simulations, a double nesting procedure was employed. The coarsest nest at  $0.0625^\circ$   
131 resolution (about 7 km) covers 250 grid points in x direction and 250 grid points in y  
132 direction. The size and location of the 7 km domain has been considered large enough  
133 to take into consideration all possible synoptic situations relevant for the development  
134 of extreme phenomena in the study area as well as the influence of the Mediterranean  
135 Sea. The finest nest at  $0.025^\circ$  (circa 2.8 km) covers 150 x 150 grid points, thus a total  
136 area of 22500 grid points and includes the study area (72 grid point in x direction and  
137 92 in y direction) centred around the Dead Sea.

138 A Tiedtke (1989) mass-flux scheme is used for moist convection in the 7 km, and  
139 reduced Tiedtke mass-flux scheme for shallow convection. Contrary to the CCLM-7 km  
140 simulation, where convection is parameterized, in the CCLM-2.8 km convection is  
141 explicitly resolved (Doms and Baldauf, 2015), so only the reduced Tiedtke mass-flux  
142 scheme is used for shallow convection. The model physics includes a cloud physics  
143 parameterization with 5 types of hydrometeors (water vapor, cloud water, precipitation  
144 water, cloud ice, precipitation ice), a radiative transfer scheme based on a delta-two-  
145 stream solution (Ritter and Geleyn, 1992) and a roughness-length dependent surface  
146 flux formulation based on modified Businger relations (Businger et al., 1971).

147 Orography data from GLOBE (Global Land One-km Base Elevation Project) of NOAA  
148 (National Oceanic and Atmospheric Administration) and soil data from HWSD  
149 (Harmonized Worlds Soil Database) TERRA is used. HWSD is a global harmonization  
150 of multiple regional soil data sets with a spatial resolution of 0.008° (FAO, 2009),  
151 resulting in 9 different soil types in the model, namely 'ice and glacier', 'rock / lithosols',  
152 'sand', 'sandy loam', 'loam', 'loamy clay', 'clay', 'histosols', and 'water'.

153 Multiple model runs have been performed. A 7 km run from 2003 to 2013 with daily  
154 output is used as nesting for two 2.8 km runs over the same time span. The Dead Sea  
155 is dried out and replaced with soil types from the surrounding area in one of them  
156 (SEN), the other one is used as reference (CLIM). For the detailed investigation of  
157 convective events on 14.11.2011 and 19.11.2011, sub-seasonal simulations have been  
158 performed with the same settings as the decadal simulation, but with additional hourly  
159 output.

## 160 **2.2 Methodology**

161 A decadal simulation covering the 2003 to 2013 time period was carried out with the  
162 convection permitting 2.8 km COSMO-CLM model. Lateral boundary conditions and  
163 initial conditions are derived from the European Centre for Medium-Range Weather  
164 Forecasts (ECMWF) data. The COSMO-CLM 7 km is used as nesting step in between  
165 the forcing data and the 2.8 km run. This reference or Dead Sea simulation, will be  
166 hereafter referred to as REF<sup>CLIM</sup> simulation. Parallel to this, an idealized sensitivity  
167 experiment (hereafter SEN<sup>CLIM</sup> or bare soil simulation) is carried out in which the Dead  
168 Sea conditions are set to bare soil on -405 m level (depth of the Dead Sea in the  
169 external data set, GLOBE (Hastings and Dunbar, 1999)). After examination of the  
170 results, the first year of simulations is considered spin-up time, thus, our analysis  
171 covers the 2004-2013 period.

172 The precipitation field has been validated using the EOBS dataset (resolution of 0.1°  
173 and available for the period 1980-2011; Haylock et al. 2008), and the APHRODITE's  
174 (Asian Precipitation - Highly-Resolved Observational Data Integration Towards  
175 Evaluation: Yatagai et al. 2008, 2012) daily gridded precipitation, resolution of 0.25°  
176 and available for 1980-2007. The APHRODITE data shows generalized lower  
177 precipitation values than EOBS, but still higher than our simulation particularly close to  
178 the northern Mediterranean shoreline, over coastal-flat terrain, whereas the best  
179 agreement is at areas dominated by complex terrain. Despite these biases the  
180 comparison of the temporal areal-mean of the model simulations at 7 km and 2.8 km  
181 and the APHRODITE dataset demonstrates that in general the model quite well  
182 captures the precipitation events. An improvement is seen at the finer resolution.

183 Regional dry and wet periods are identified and quantified in the simulations by means  
184 of the Effective Drought Index (EDI; Byun and Wilhite 1999; Byun and Kim 2010). The  
185 EDI is an intensive measure that considers daily water accumulations with a weighting  
186 function for time passage normalizing accumulated precipitation. The values are  
187 accumulated at different time scales and converted to standard deviations with respect  
188 to the average values. Here we use an accumulation period of 365 days. EDI dry and  
189 wet periods are categorized as follows: moderate dry periods  $-1.5 < \text{EDI} < -1$ , severe dry  
190 periods  $-2 < \text{EDI} < -1.5$ , and extreme dry periods  $\text{EDI} < -2$ . Normal periods are revealed by  
191  $-1 < \text{EDI} < 1$  values.

192 Based on daily mean values, precipitation and evapotranspiration distribution and  
193 possible tendencies in the 10-year period are assessed. To further assess the most  
194 affected areas in our study area, this is divided in four subdomains surrounding the  
195 Dead Sea and trying to respect the orographic pattern in the area (Figure 3). Annual  
196 cycles are thus separately investigated to take into consideration the relevant  
197 differences in orography, soil types, and distance to the coast among others (Figure1),  
198 which are known to have a significant impact in the precipitation distribution in the  
199 region (e.g. Belachsen 2017; Houze 2012). . Differences in the annual cycle and  
200 temporal evolution of precipitation and evapotranspiration between the  $\text{REF}^{\text{CLIM}}$  and  
201  $\text{SEN}^{\text{CLIM}}$  are discussed. Also, differences in the near-surface and boundary layer  
202 conditions and geopotential height patterns are examined. Geographical patterns of  
203 mean evapotranspiration and precipitation and differences with respect to the reference  
204 or Dead Sea simulation are assessed. Probability distribution functions (PDFs), and the  
205 Structure, Amplitude and Location (SAL: Wernli et al. 2008) analysis methodologies are  
206 used to illustrate differences in the mean and extreme precipitation between the  
207 reference and the sensitivity experiments. The SAL is an object-based rainfall

208 verification method. This index provides a quality measure for the verification of  
209 quantitative precipitation forecasts considering three relevant aspects of precipitation  
210 pattern: the structure (S), the amplitude (A), and the location (L). The A component  
211 measures the relative deviation of the domain-averaged rainfall; positive values  
212 indicate an overestimation of total precipitation, negative values an underestimation.  
213 The component L measures the distance of the center of mass of precipitation from the  
214 modelled one, and the average distance of each object from the center of mass. The  
215 component S is constructed in such a way that positive values occur if precipitation  
216 objects are too large and/or too flat and negative values if the objects are too small  
217 and/or too peaked, quantifying the physical distance between the centres of mass of  
218 the two rainfall fields to be compared. Perfect agreement between prediction and  
219 reference are characterized by zero values for all components of SAL. Values for the  
220 amplitude and structure are in the range  $(-2, 2)$ , where  $\pm 0.66$  represents a factor of 2  
221 error. The location component ranges from 0 to 2, where larger values indicate a  
222 greater separation between centres of mass of the two rainfall fields. This is done by  
223 selecting a threshold value of 1/15 of the maximum rainfall accumulation in the domain  
224 (following Wernli et al. 2008). The structure and location components are thus  
225 independent of the total rainfall in the domain.

226

227 Differences in the temporal evolution of precipitation between the REF<sup>CLIM</sup> and SEN<sup>CLIM</sup>  
228 are identified. In Table 1, those events in which an area-mean (study area, Figure 1)  
229 difference between both simulations higher than  $\pm 0.1$  mm/d exists are selected as  
230 potential heavy precipitation events and classified attending to their synoptic scale  
231 environment and atmospheric stability conditions (Table 1).

232 Although Dayan and Morin (2006) discuss that in general large-scale vertical motions  
233 do not provide the sufficient lifting necessary to initiate convection, it was demonstrated  
234 by Dayan and Sharon (1980) that a relationship exists between the synoptic-scale  
235 weather systems and deep moist convection, being those systems responsible for the  
236 moisturizing and destabilization of the atmosphere prior to convective initiation. They  
237 pointed out that indices of instability proved the most efficient determinants of the  
238 environment characterizing each rainfall type in the region. Thus, two indicators of the  
239 atmospheric degree of stability/instability, namely the Convective Available Potential  
240 Energy (CAPE; Moncrieff and Miller 1976) and the KO-index (Andersson et al. 1989),  
241 are examined in this study. The CAPE is a widely known index indicating the degree of  
242 conditional instability. Whereas, the KO-index, which is estimated based on the  
243 equivalent potential temperature at 500, 700, 850 and 1000 hPa (following the



244 recommendations by Bolton 1980), describes the potential of deep convection to occur  
245 as a consequence of large-scale forcing (Andersson et al. 1989; Khodayar et al. 2013).  
246 Generally, regions with KO-index  $< 2$  K and large-scale lifting are identified as  
247 favourable for deep convection. Parcel theory (50 hPa ML (Mixed Layer) parcel) and  
248 virtual temperature correction (Doswell and Rasmussen 1994) are applied to these  
249 calculations.

250 Based on the above criteria, a separation was made between events with widespread  
251 rainfall and those more localized. Among the latter, we selected two events to illustrate  
252 the local impacts on the boundary layer conducive to deep moist convection.  
253 Particularly, differences in the amount, structure and location of precipitation are  
254 assessed by examining the spatial patterns and the SAL verification method. The two  
255 selected events for detail analysis in this study are those showing the larger SAL  
256 deviations. Those two cases occur close in time, but they are not the same event. No  
257 differences in the soil and atmospheric conditions have been found in the period  
258 between the events when the REF and SEN simulations are compared. Even though  
259 a more detail analysis is provided for the two selected cases, all convective-events  
260 listed in Table 1 have been examined to assess the main impacts on the mechanisms  
261 leading to convection. High-resolution simulations with the NWP COSMO 2.8 km model  
262 are performed with hourly output temporal resolution and covering a 3-day period  
263 (including 48-h prior to the day of the event, from 00 UTC) to capture atmospheric pre-  
264 conditions conducive to deep moist convection. For this, a reference simulation,  
265 REF<sup>NWP</sup> or Dead Sea simulation, and a sensitivity experiment, SEN<sup>NWP</sup> or bare soil  
266 simulation, are carried out for each event.

267 We have to point out that the external data sets commonly employed describing  
268 relevant features of the Dead Sea region, such as the depth, shape and orography of  
269 the Dead Sea, as well as Dead Sea water characteristics at the reference or Dead Sea  
270 run, do not accurately represent the reality. In the same direction, biases in relation to  
271 different variables such as the precipitation field and evaporation over the Dead Sea  
272 have to be considered.

273

### 274 **3. Results and discussion**

#### 275 **3.1 Climatology of the Dead Sea region**

276 *Annual cycle*

277 To assess the climatology of the study region (Figure 1) the annual evaporation and  
278 precipitation cycles based on daily means of the respective quantities are investigated  
279 (Figure 2). Additionally, we examine the evolution of specific humidity ( $Q_{v_{2m}}$ ) and  
280 temperature at 2 m ( $T_{2m}$ ) as well as total column integrated water vapour (IWV) and  
281 low-boundary layer ( $< 900$  hPa) equivalent potential temperature ( $\Theta_e$ ). Possible  
282 changes in the atmospheric stability conditions are evaluated by examination of the  
283 CAPE and KO-index. In Figure 2, all grid points over the study region (Figure 1) and  
284 the time period 2004-2013 are considered. Differences between the REF<sup>CLIM</sup> and the  
285 SEN<sup>CLIM</sup> simulations are also discussed.

286 The annual cycle of evaporation shows minimum values in the autumn season (around  
287 October,  $\sim 0.1$  mm/d) and maximum evaporation in spring (around March,  $\sim 0.4$  mm/d).  
288 The dependency with the precipitation cycle is clear with maximum values of the latter  
289 around March and rain occurring between October and May (Figure 2a) in agreement  
290 with observations in the area (Dayan and Sharon 1980). The difference between the  
291 evaporation in the REF<sup>CLIM</sup> and the SEN<sup>CLIM</sup> simulations indicates a mean decrease in  
292 the order of 0.02 (February) to  $\sim 0.1$  (August) mm/d in the absence of the Dead Sea  
293 water (SEN<sup>CLIM</sup>). The largest difference is in the dry period (May to October) when  
294 water availability is less dependent on precipitation, and evaporation is higher over the  
295 Dead Sea in contrast to the minimum values over land (Metzger et al. 2017). In  
296 general, there is a decrease of about 0.5 % in mean precipitation in the SEN<sup>CLIM</sup>  
297 simulation. In contrast to the differences in evaporation, precipitation differences  
298 between the reference or Dead Sea simulation and the sensitivity or bare soil  
299 simulation occur in both directions during the rain period, from October to May.  
300 Examining the total number over the whole decadal simulation it is seen that the  
301 number of dry or wet days ( $> 0.1$  mm/d) or heavy precipitation events is not largely  
302 affected in the bare soil simulation. In general, the number of dry days increases (fewer  
303 wet days) in the SEN<sup>CLIM</sup> simulation, whereas the number of high intensity events show  
304 almost no variation. For each simulation, the difference between precipitation and  
305 evaporation is negative mainly in spring and summer contributing to the dryness in the  
306 region. Furthermore, the difference between the REF<sup>CLIM</sup> and SEN<sup>CLIM</sup> simulations  
307 indicates that PREC-EVAP is higher in the SEN<sup>CLIM</sup> simulation probably in relation to  
308 the reduced evaporation over the dry sea area and the general decrease in the  
309 precipitation amount in the region.

310 In addition to the reduced evaporation and precipitation (about 0.5 %) in the whole  
311 domain in the SEN<sup>CLIM</sup> simulation a drier and warmer lower-troposphere is identified  
312 (Figure 2b) in agreement with the observational assessment by Metzger et al. (2017) of

313 the cooling effect of evaporation on air temperature in the region. The annual cycle of  
314 IWV and  $\Theta_{e<900hPa}$  in Figure 2c show that the impact of the dry Dead Sea resulting  
315 evaporation is less pronounced when a deeper atmospheric layer is considered.  
316 Indeed,  $\Theta_{e<900hPa}$  evolution evidences that the warming effect due to the decreased  
317 evaporation in the SEN<sup>CLIM</sup> simulation is restricted to the near surface.

318 In Figure 2d, the annual cycle of areal mean CAPE displays larger values in the period  
319 from August to November, being this the period more favourable for convection.  
320 Negative CAPE differences between the REF<sup>CLIM</sup> and the SEN<sup>CLIM</sup> simulations are  
321 presumably in relation to the identified distinct lower-atmospheric conditions, being  
322 these more favourable and consequently CAPE values higher in the REF<sup>CLIM</sup>  
323 simulation. In the same period, the KO-index indicates a more potentially unstable  
324 atmosphere, i.e. prone to deep convection because of large-scale forcing, and larger  
325 differences between simulations.

326 In agreement with the well-known precipitation distribution in the region most of the  
327 events occur in A1 (north-west) and A2 (north-east). Also, in these subdomains larger  
328 differences between the REF<sup>CLIM</sup> and SEN<sup>CLIM</sup> simulations are identified pointing out the  
329 relevance of the Dead Sea evaporation in the pre-convective environment for rainfall  
330 episodes over the study area (Figure3a). Considering only land grid points almost no  
331 difference between simulations is found in the evaporation annual cycle of A1 and A2  
332 (Figure3b) suggesting the distinct amount of moisture advected towards A1 and A2  
333 from the Dead Sea in REF<sup>CLIM</sup> and SEN<sup>CLIM</sup> as responsible for the differences in the  
334 boundary layer conditions conducive to convection. Also, in these subdomains the  
335 dryer and warmer lower boundary layer and the reduced instability in the SEN<sup>CLIM</sup> are  
336 recognized

### 337 *Inter-annual variability*

338 In Figures 4 we discuss the inter-annual variability (based on monthly-daily areal mean  
339 values) of evaporation, precipitation as well as drought evolution.

340 The reduced evaporation in the annual cycle of the SEN<sup>CLIM</sup> simulation for the whole  
341 investigation domain, resulting from the drying of the Dead Sea and affected  
342 evaporation, remains from year to year (Figure 4a). Larger differences between the  
343 simulations occur in the May to November months in agreement with the annual cycle  
344 in Figure 2a. This, and the time period of the maximum/minimum is constant over the  
345 years. A tendency towards lower evaporation at each simulation and higher differences  
346 between both at the end of the period are identified. An inter-annual fluctuation is

347 observed in both REF<sup>CLIM</sup> and SEN<sup>CLIM</sup> simulations. The yearly rate of evaporation  
348 shows, for example, in REF<sup>CLIM</sup> maximum values of about 7 mm in 2011 and around 17  
349 mm in 2012. This is in agreement with the positive correlation expected between  
350 precipitation and evaporation, a trend towards decreased precipitation and a  
351 correspondence between drier years such as the 2011-2012 period and lower annual  
352 evaporation are seen in Figure 4b. Year to year EDI calculations in Figure 4c help us  
353 identify the regional extreme dry and wet periods. The EDI range of variation from  
354 about -1 to 2 for the whole period of simulation indicates that the dry condition is the  
355 common environment in the area, while the wet periods, EDI up to 6, could be  
356 identified as extreme wet periods (relative to the area), in this case in the form of heavy  
357 precipitation events. Maximum positive EDI values are in the first months of the year in  
358 agreement with the precipitation annual cycle in Figure 2, whereas minimal EDI values  
359 occur in summer and autumn indicative of the dry conditions in these periods.  
360 Differences in the EDI calculations from both simulations reveal distinct precipitation  
361 evolutions and denote timing differences in the occurrence of the precipitation events.  
362 When the regional climate evolution is examined in combination with the impact on the  
363 number of heavy precipitation events (Table 1) the impact is stronger in the dry period  
364 of 2011 (Figure 4a). About six events show relevant differences in this period, contrary  
365 to the average 3 episodes per year.

### 366 *Spatial distribution*

367 The geographical patterns of evaporation and precipitation are presented in Figure 5.  
368 Over the Dead Sea, the simulated average annual evaporation for the period under  
369 consideration is in the order of 1500-1800 mm/y, in contrast to the values in the deserts  
370 east and south, where the evaporation is less than 20 mm/y. Observed annual  
371 evaporation of this lake is known to be about 1500 mm and to vary with the salinity at  
372 the surface of the lake and freshening by the water inflow (Dayan and Morin 2006;  
373 Hamdani et al. 2018). Over land, higher evaporation is seen over the Judean  
374 Mountains and the Jordanian Highlands. High correlation with the orography and soil  
375 types is seen (Figure 1). Evaporation is probably correlated with rainfall which in turn is  
376 correlated with topography. Particularly, in the Jordanian Highlands where maximum  
377 evaporation is around 200 mm/y, the complex topography coincides with sandy loam  
378 soils, whereas most of the soil in study region is defined as loamy clay or clay (Figure  
379 1). The evaporative difference field between simulations in Figure 5a shows a highly  
380 inhomogeneous patchiness not evidencing any relationship with orography or soil type,  
381 but rather with changes in the precipitation pattern in the SEN<sup>CLIM</sup> simulation as seen in  
382 Figure 5b.

383 In agreement with the temporal series of areal mean precipitation in Figure 3 higher  
384 annual precipitation are in the north-west and -east, with respect to the southern  
385 regions. Topographic features exert a large impact on precipitation distribution with  
386 maxima of about 175 to 300 mm/y over the Judean Mountains and the Jordanian  
387 Highlands. To the northern end of the Dead Sea valley, the largest precipitation  
388 difference between the REF<sup>CLIM</sup> and the SEN<sup>CLIM</sup> simulations is identified, rather than  
389 directly over the Dead Sea area noting the importance of advected moisture from the  
390 Dead Sea evaporative flux upslope and along the Dead Sea valley as well as the  
391 indirect effects of a different spatial distribution of low-tropospheric water vapour in the  
392 occurrence of precipitating convection.

393 Regarding the impact on the large-scale conditions, differences in the spatial pattern  
394 and strength of the 500 hPa geopotential height field are identified over the Dead Sea  
395 (not shown). In the 10-year mean, differences up to 0.002gpdm higher in SEN than in  
396 REF are observed. Around the Dead Sea area, the differences are smaller and more  
397 irregular. Generally, the differences are higher in the east of the Dead Sea than in the  
398 west.

#### 399 *Precipitation probability distribution function*

400 While the probability for lower intensity precipitation is very similar in the REF<sup>CLIM</sup> and  
401 the SEN<sup>CLIM</sup> simulations differences are recognized in the higher precipitation  
402 intensities, from about 150 mm/d (Figure 6a). Particularly, above 180 mm/d extreme  
403 precipitation values occur less frequent at the SEN<sup>CLIM</sup> simulation where a drier,  
404 warmer and more stable atmosphere is identified (Figure 2).

#### 405 *SAL*

406 The use of the SAL method in this study differs from the approach frequently presented  
407 in literature since it is here not our purpose to examine differences between the  
408 simulated field and observations (adequate observations for this comparison are not  
409 available in the area), but to compare changes regarding the structure, amount and  
410 location of the precipitation field between our reference or Dead Sea simulation and  
411 sensitivity or bare soil simulation experiments. Figure 6b shows that when the mean  
412 precipitation over the whole simulation period is considered all three SAL components  
413 are close to zero, meaning that very small differences are found. However, when single  
414 precipitation events in the REF<sup>CLIM</sup> simulation are compared with the same period at the  
415 SEN<sup>CLIM</sup> simulation, larger differences regarding structure, amount and location of  
416 rainfall events are found. For further examination of this issue two exemplary heavy

417 precipitation events (indicated by boxes in Figure 6b) are analysed in detail. In both  
418 cases, a negative A-component is recognized, that is, less precipitation falls in the  
419 SEN<sup>CLIM</sup> simulation. The S-component also evidences the change in the structure of the  
420 convective cells. The L-component is low meaning that the convective location does  
421 not change significantly in the SEN<sup>CLIM</sup> simulation, in contrast to the intensity and  
422 structure of the cells.

423

### 424 **3.2 Sensitivity of atmospheric conditions to the Dead Sea drying: episodic** 425 **investigation**

426 Among those events exhibiting differences in the precipitation field between both  
427 simulations (Table 1 and Figure 6b) two situations occurring in the time period of the 14  
428 to 19 November 2011 are investigated in the following.

429 In this term, the synoptic situation is characterized by a Cyprus low and its frontal  
430 system located over the Dead Sea at about 00 UTC on the 15 November 2011 and at  
431 12 UTC on the 18 November 2011. The low-pressure system and its frontal system  
432 induced strong south-westerly to westerly winds with mean wind velocities up to 15  
433 m/s.

434 In the first situation (hereafter CASE1), in association with the western movement of  
435 the cold front a convective system develops over the Jordanian Highlands with  
436 precipitation starting at about 21 UTC on the 14 November 2011. This convective  
437 system is of high interest because of the large difference in its development between  
438 the REF<sup>14.11</sup> and the SEN<sup>14.11</sup> simulations.

439 In Figure 7a the 24-h accumulated precipitation, from 14.11 09 UTC to 15.11 08 UTC,  
440 in the investigation area is shown for the REF<sup>14.11</sup> and the SEN<sup>14.11</sup> simulations. Two  
441 precipitation areas are seen, on the north-western and north-eastern of the Dead Sea.  
442 Larger difference between models is on the north-eastern region (24-h accumulated  
443 precipitation > 100 mm/d in REF<sup>14.11</sup>, while < 50 mm/d in SEN<sup>14.11</sup>), which is the focus of  
444 our analysis.

445

446 The REF<sup>14.11</sup> simulation shows that in the 6 hours period prior to the initiation of  
447 convection the pre-convective atmosphere and more specifically the lower boundary  
448 layer exhibit a moist (IWV ~ 24-30 mm, qvPBLmax ~ 7-10 g/kg) and unstable (CAPE ~  
449 1100 J/kg; KO-index ~ -8 K; not shown) air mass on the western side of the  
450 investigation area, particularly close to the western Mediterranean coast, and drier

451 (IWV~ 8-16; qvPBLmax ~ 4-6 g/kg) and more stable conditions (CAPE< 200 J/kg; KO-  
452 index ~ 0-2 K) on the eastern side of the domain (Figure 7b). A maximum difference of  
453 about 5 g/kg from west to east is established in the lower boundary layer.

454 Main differences between both simulations are over the Dead Sea (IWV difference up  
455 to 2 mm and qvPBL up to 1.5 g/kg) and north and north-east of it, but almost similar  
456 conditions everywhere else. In our target area (subdomain of investigation where the  
457 convection episode takes place (red box in Figure 7)), north-east of the Dead Sea, a  
458 drier and a more stable atmosphere is identified at the SEN<sup>14.11</sup> simulation.

459 The evolution of the wind circulation systems in the area is similar in both simulations  
460 (Figure 7c). The 700 hPa, 850 and 950 hPa winds dominantly blow from the south  
461 south-west during the pre-convective environment advecting the moist unstable air  
462 mass towards the Dead Sea valley and north-east of it, directly affecting the  
463 atmospheric conditions at the target area (for a comparison with a climatology of the  
464 wind conditions in the region please see Metzger et al. 2017). In both simulations, the  
465 passage of the cold front over the Dead Sea establishes a strong southerly wind from  
466 about 10 UTC on the 14 November 2011.

467 Prior to this time, dry air was advected below about 850 hPa towards the target area  
468 from the east. The turning of the low-level winds and the resulting moistening of the  
469 atmosphere is well and equally captured by both simulations (Figure 8a). Furthermore,  
470 at the near-surface, from about 16 UTC, ~ 5 h prior to convection initiation in the target  
471 area, a near-surface convergence line forms at the foothills of the northern part of the  
472 Jordanian Highlands, which is also well and equally captured by both simulations  
473 (Figure 8b). The lifting provided by the convergence line triggers convection in the  
474 area. However, the drier and more stable atmosphere in the SEN<sup>14.11</sup> simulation results  
475 in less intense convection, weaker updrafts, and reduced precipitation at the eastern  
476 slope of the valley.

477

478 In the second case, CASE2, we address an episode of localized convection taking  
479 place on the north-western edge of the Dead Sea in the REF simulation, whereas no  
480 convection develops in the SEN simulation. The isolated convection in the REF  
481 simulation left about 50 mm rain in 3 h starting at about 03 UTC on the 19 November  
482 2011 (Figure 9).

483 In contrast to CASE1, the modification of the pre-convective environment relevant for  
484 convective initiation is in this case dominated by dynamical changes in the mesoscale  
485 circulations. Differences in the evolution and strength of the Mediterranean Sea Breeze  
486 (MSB), the Dead Sea breeze and orographic winds influence atmospheric conditions in

487 the target area leading to the assistance to or to the absence of convection. The most  
488 significant difference observed between the simulations is in the development of a  
489 strong near-surface convergence line in the REF simulation (which is not present in the  
490 SEN simulation hindering convection in the area), which forms about 2 h before  
491 convective initiation (Figure 10).

492 Even in the first hours of the 18 November 2011 differences in the speed and direction  
493 of the near-surface winds over the Dead Sea and on the eastern flank of the Jordanian  
494 Highlands could be identified. A fundamental difference between simulations occurs  
495 from about 17 UTC when strong westerly winds indicating the arrival of the MSB reach  
496 the western shore of the Dead Sea. One hour later, in the REF<sup>19,11</sup> run the MSB  
497 strongly penetrates the Dead Sea valley reaching as far as the eastern coast in the  
498 centre to south areas. However, in the SEN<sup>19,11</sup> simulation the MSB does not penetrate  
499 downward, instead strong northerly winds flow along the valley (Figure 10a). Numerous  
500 observational and numerical studies carried out to investigate the dynamics of the MSB  
501 (e.g. Naor et al. 2017; Vuellers et al. 2018) showed that the downward penetration of  
502 the MSB results from temperature differences between the valley air mass, which is  
503 warmer than the maritime air mass. An examination of temperature differences along a  
504 near-surface north-south valley transect (positions in Figure 10a) indicates a decrease  
505 of about 4 °C at the near-surface over the dried Dead Sea area in contrast to negligible  
506 changes on a parallel transect inland, on the western coast of the Dead Sea. These  
507 evidences the notorious impact of the absence of water in the valley temperature, thus,  
508 gradients in the region. The colder valley temperatures do not favour the downward  
509 penetration of the MSB, which strongly affects the atmospheric conditions in the valley.  
510 Moreover, a north-easterly land breeze is visible from about 20 UTC on the eastern  
511 shore of the Dead Sea in the REF<sup>19,11</sup> simulation, but not in the SEN<sup>19,11</sup> simulation  
512 (Figure 10b). This situation reflects an interesting case different from the ones  
513 generally presented in former investigations in the area (e.g. Alpert et al. 1997 ; and  
514 Alpert et al. 2006b) in which due to the recent weakening of the Dead-Sea breeze,  
515 mainly because of the drying and shrinking of the Sea, the Mediterranean breeze  
516 penetrates stronger and earlier into the Dead-Sea Valley increasing the evaporation  
517 because of the strong, hot and dry wind.

518 Mountain downslope winds develop in both simulations from about 22 UTC. One hour  
519 later, strong northerly valley flow in the northern part of the Dead Sea contrasts with the  
520 westerly flow in the SEN<sup>19,11</sup> simulation (Figure 10c). As the valley cools down during  
521 night time in the SEN simulation, T2m decreases about 1 K from 20 UTC to 03 UTC in  
522 contrast with the 0.1 K decrease of the Dead Sea in the REF simulation, the



523 temperature gradient weakens and the northerly valley flow present in the REF  
524 simulation is absent in the SEN simulation. During the night, the synoptic conditions  
525 gain more influence than the local wind systems governing the conditions in the valley  
526 during day time. South-easterly winds prevail in the valley in both simulations. Much  
527 stronger wind velocities are reached in the REF simulation, confirming the sensitivity of  
528 large-scale dynamics to near-surface climate change-induced impacts.

529 The encounter of the north north-westerly and south south-easterly winds over the  
530 Dead Sea area in the REF<sup>19,11</sup> simulation induces the formation of a convergence zone,  
531 which intensifies and extends offshore over the next hours and determines the location  
532 of convective initiation. Meanwhile, homogeneous south-easterly winds are observed in  
533 the SEN simulation (Figure 10d).

534 The differences in the wind circulations contribute to a different distribution of the  
535 atmospheric conditions in the target area, particularly, low-tropospheric water vapour  
536 as seen in the vertical cross sections in Figure 11. The evolution of the atmospheric  
537 conditions in the 3-h period prior to convective initiation evidences the deeper and  
538 wetter boundary layer in the REF<sup>19,11</sup> simulation at the north-western foothills of the  
539 ridge at the Jordanian Highlands. Differences of IWV up to 2 mm, and of instability  
540 (CAPE) close to 200 J/kg are found in this area (not shown). This is the location of the  
541 convergence line where convective updrafts, which start close to the ground, are  
542 triggered reaching a maximum vertical velocity of about 5 m/s above the convergence  
543 zone in the REF<sup>19,11</sup> simulation.

544

#### 545 **4. Conclusions**

546 The drying and shrinking of the Dead Sea has been extensively investigated in the last  
547 decades from different points of view. This process has been related to significant local  
548 climate changes which affect the Dead Sea valley and neighboring regions. The  
549 climate of the Dead Sea is very hot and dry. But occasionally the Dead Sea basin is  
550 affected by severe convection generating heavy precipitation, which could lead to  
551 devastating flash floods.

552 In this study, high-resolution COSMO model simulations are used to assess the  
553 sensitivity of Dead Sea changes on the occurrence of convective precipitation in the  
554 region. A set of high-resolution, ~ 2.8 km, climate simulations covering the period 2003  
555 to 2013, and several numerical weather prediction (NWP) runs on an event time scale  
556 (~ 48-36 h) are performed over the Dead Sea area. On a decadal time scale, two

557 simulations are carried out. The first “reference or Dead Sea” run, and a second  
558 idealized run “sensitivity or bare soil” in which the Dead Sea is set to bare soil. The  
559 NWP simulations focus on two heavy precipitation events exhibiting relevant  
560 differences between the reference or Dead Sea and the sensitivity or bare soil decadal  
561 runs. A total of four simulations are performed in this case.

562 As the energy balance partitioning of the Earth’s surface changes after setting the  
563 Dead Sea area to bare soil conditions, relevant impacts could be identified in the  
564 region. From a climatological point of view, less evaporation, higher air temperatures  
565 and less precipitation (about 0.5 %) are observed. Reduced evaporation over the Dead  
566 Sea occurs from May to October. Atmospheric conditions, such as air temperature and  
567 humidity, are mostly affected in the lower-tropospheric levels, which in turn influence  
568 atmospheric stability conditions, hence, precipitating convection. In general, the  
569 number of dry/wet days is not largely affected by the changed conditions of the Dead  
570 Sea, although these differences could be larger for hourly precipitation; rather the  
571 structure and intensity of the heavier precipitation events is changed. While a general  
572 and homogeneous decrease in evaporation is seen at the SEN<sup>CLIM</sup> simulation,  
573 precipitation deviations occur in both directions, which could suggest and impact on the  
574 timing of the events. A relevant year to year variability is observed in evaporation-  
575 precipitation which indicates the need of long time series of observations to understand  
576 local conditions and to validate model simulations.

577 The detailed analysis of two heavy precipitation events allowed us to further assess the  
578 possible causes and the processes involved regarding the decrease in precipitation  
579 intensity or the total omission of convection with respect to the reference or Dead Sea  
580 simulation in the absence of the Dead Sea water. Two main components, strongly  
581 affected by the changed conditions of the Dead Sea area, are found to be highly  
582 relevant for the understanding of the environmental processes in the Dead Sea region.

583 (a) First, the lower-atmospheric boundary layer conditions. Changes in the energy  
584 balance affect the atmosphere through the heat exchange and moisture supply. The  
585 drying of the Dead Sea in the SEN simulations and the resulting decrease in local  
586 evaporation, impact the Dead Sea Basin conditions and the neighbouring areas. A  
587 reduction in boundary layer humidity and an increase in temperature result in a general  
588 decrease of atmospheric instability and weaker updrafts indicating reduced deep-  
589 convective activity. Main differences on the atmospheric conditions are directly over the  
590 Dead Sea, but these conditions are frequently advected to neighbouring areas by the

591 thermally driven wind systems in the region which play a key role for the redistribution  
592 of these conditions and the initiation of convection.

593 (b) Secondly, wind systems in the valley. In the arid region of the Dead Sea Basin with  
594 varied topography, thermally and dynamically driven wind systems are key features of  
595 the local climate. Three different scales of climatic phenomena coexist: The  
596 Mediterranean Sea Breeze (MSB), the Dead Sea breeze and the orographic winds,  
597 valley-, and slope-winds, which are known to temper the climate in the Dead Sea valley  
598 (Shafir and Alpert, 2011). The drying of the Dead Sea in the SEN simulation disturbs  
599 the Dead Sea thermally driven wind circulations. The Dead Sea breezes are missing,  
600 weaker wind speeds characterize the region and along valley winds are consequently  
601 affected. Furthermore, the dynamics of the Mediterranean breeze penetration into the  
602 Jordan Valley are affected.

603

604 Consequently, the impacts on convection initiation and development are twofold:

605 (i) Distinct redistribution of atmospheric conditions, locally or remotely, which yields to  
606 different atmospheric conditions that in the absence of the Dead Sea result in a  
607 reduced moisture availability in the lower atmospheric levels and increased stability  
608 hindering convection or reducing the intensity of the events.

609 (ii) Modification of the divergence/convergence field. The absence of the Dead Sea  
610 substantially modifies the wind circulation systems over the Dead Sea valley, which  
611 leads to the omission of convergence lines which act as triggering mechanism for  
612 convection.

613

614 We can conclude that in general the lack of sufficient low-atmospheric moisture, the  
615 increase of atmospheric stability in addition to an absence or reduction in the intensity  
616 of the convergence zones, works against initiation or intensification of precipitating  
617 convection in the area. The relevance of the small-scale variability of moisture and the  
618 correct definition and location of convergence lines for an accurate representation of  
619 convective initiation illustrates the limitation and the lack of adequate observational  
620 networks in the area and the need for high-resolution model simulations of boundary  
621 layer processes to predict intense and localised convection in the region.

622 These results contribute to gain a better understanding of the sensitivity of local  
623 conditions in the Dead Sea valley and neighbouring areas to changing conditions at the  
624 Dead Sea. Energy balance partitioning and wind circulation systems are determinant  
625 for local climatic conditions, e.g. temperature and humidity fields as well as aerosol  
626 redistribution, therefore, any change should be well understood and properly

627 represented in model simulations of the region. Our results point out, in agreement with  
628 past modelling activities in the region, the need to further improve the representation of  
629 precipitation fields in the area, particularly close to the Mediterranean coastline. More  
630 accurate Mediterranean SST input fields have been suggested as relevant to reduce  
631 the model inaccuracies. Furthermore, a more realistic representation of the lake shape,  
632 water salinity and temperature, as well as Dead Sea abundance and depth must be  
633 addressed to more accurately describe present and expected future conditions. In the  
634 present study, limitations found in this direction in relation to model and external data  
635 set descriptions, as well as identified biases regarding for example moisture sources  
636 for HP in the region, MSB and Dead Sea evaporation, are expected to impact our  
637 results, and have to be improved in future efforts in the region. In a further step, the  
638 authors will investigate some of these issues in more detail, and will assess the impact  
639 of model grid resolution on the horizontal and vertical flow field in the region across  
640 scales, including the impact on large-scale dynamics. We will also put emphasis in  
641 trying to better understand the dynamics of the MSB using high-resolution modelling,  
642 especially the contrasting behaviour pointed out in this study. Fine resolution  
643 simulations up to 100 m will be performed for this purpose. Furthermore, we will  
644 provide a verification of the complex chain of processes in the area using unique  
645 measurements in the framework of the interdisciplinary virtual institute Dead Sea  
646 Research VEnue (DESERVE; Kottmeier et al., 2016).

647

#### 648 **Author contribution**

649 SK wrote the manuscript, analysed the data, interpreted the results and supervised the  
650 work. JH carried out data analysis, interpretation of results and prepared all the figures.

651

#### 652 **Acknowledgements**

653 The first author's research was supported by the Bundesministerium für Bildung und  
654 Forschung (BMBF; German Federal Ministry of Education and Research). The authors  
655 acknowledge the colleagues at the Karlsruhe Institute of Technology (KIT) involved in  
656 the interdisciplinary virtual institute Dead Sea Research VEnue (DESERVE) for their  
657 support and interesting discussions. We acknowledge Sebastian Helgert and Alberto  
658 Caldas Alvarez for their assistance in the preparation of the simulations. This article is  
659 a contribution to the HyMeX program.

661 **References**

- 662 Alpert, P., and Shay-EL, Y.: The Moisture Source for the Winter Cyclones in the  
663 Eastern Mediterranean. *Israel Meteorological Research Papers*, 5, 20-27, 1994.
- 664 Alpert, P., and Coauthors: Relations between climate variability in the Mediterranean  
665 region and the tropics: ENSO, South Asian and African monsoons, hurricanes  
666 and Saharan dust. *Developments in Earth and Environmental Sciences*, 4, 149-  
667 177, [https://doi.org/10.1016/S1571-9197\(06\)80005-4](https://doi.org/10.1016/S1571-9197(06)80005-4), 2006.
- 668 Alpert, P., Shafir, H., and Issahary, D.: Recent Changes in the Climate At the Dead  
669 Sea – a Preliminary Study. *Climatic Change*, 37(3), 513-537,  
670 <https://doi.org/10.1023/A:1005330908974>, 1997.
- 671 Andersson, T., Andersson, M., Jacobsson, C., Nilsson, S.: Thermodynamic  
672 indices for forecasting thunderstorms in southern Sweden. *Meteorol. Mag.*  
673 116, 141-146, 1989.
- 674 Arkin, Y., and Gilat, A.: Dead Sea sinkholes - an ever-developing hazard.  
675 *Environmental Geology*, 39(7), 711-722,  
676 <https://doi.org/10.1007/s002540050485>, 2000.
- 677 Ashbel, D., and Brooks, C.: The influence of the dead sea on the climate of its  
678 neighbourhood. *Quarterly Journal of the Royal Meteorological Society*, 65(280),  
679 185-194, <https://doi.org/10.1002/qj.49706528005>, 1939.
- 680 Ban, N., Schmidli, J., and Schär, C.: Evaluation of the convection-resolving  
681 regional climate modeling approach in decade-long simulations, *J. Geophys.*  
682 *Res. Atmos.*, 119, 7889– 7907, <https://doi.org/10.1002/2014JD021478>, 2014.
- 683 Belachsen, I., Marra, F., Peleg, N., and Morin, E.: Convective rainfall in dry climate:  
684 relations with synoptic systems and flash-flood generation in the Dead Sea  
685 region. *Hydrology and Earth System Sciences Discussions*, 21, 5165-5180,  
686 <https://doi.org/10.5194/hess-21-5165-2017>, 2017.
- 687 Böhm, U., and Coauthors: The Climate Version of LM: Brief Description and Long-  
688 Term Applications. *COSMO Newsletter*, 6, 225-235, 2006.
- 689 Businger, J., Wyngaard, J., Izumi, Y., and Bradley, E.: Flux-Profile Relationships in the  
690 Atmospheric Surface Layer. *Journal of the Atmospheric Sciences*, 28(2), 181-

691 189, [https://doi.org/10.1175/1520-0469\(1971\)028<0181:FPRITA>2.0.CO;2](https://doi.org/10.1175/1520-0469(1971)028<0181:FPRITA>2.0.CO;2),  
692 1971.

693 Byun, H., and Kim, D.: Comparing the Effective Drought Index and the Standardized  
694 Precipitation Index. *Options Méditerranéennes. Séries A. Mediterranean*  
695 *Seminars*, 95, 85-89, 2010.

696 Byun, H., and Wilhite, D.: Objective quantification of drought severity and duration. *J.*  
697 *Climate*, 12(9), 2747-2756, [https://doi.org/10.1175/1520-](https://doi.org/10.1175/1520-0442(1999)012<2747:OQODSA>2.0.CO;2)  
698 [0442\(1999\)012<2747:OQODSA>2.0.CO;2](https://doi.org/10.1175/1520-0442(1999)012<2747:OQODSA>2.0.CO;2), 1999.

699 Cohen, S., and Stanhill, G.: Contemporary Climate Change in the Jordan Valley. *J.*  
700 *Appl. Meteor.*, 35(7), 1051-1058, [https://doi.org/10.1175/1520-](https://doi.org/10.1175/1520-0450(1996)035<1051:CCCITJ>2.0.CO;2)  
701 [0450\(1996\)035<1051:CCCITJ>2.0.CO;2](https://doi.org/10.1175/1520-0450(1996)035<1051:CCCITJ>2.0.CO;2), 1996.

702 Corsmeier, U., Behrendt, R., Drobinski, P., Kottmeier, C.: The mistral and its  
703 effect on air pollution transport and vertical mixing, *Atmos. Res.*, 74, 275–302,  
704 <https://doi.org/https://doi.org/10.1016/j.atmosres.2004.04.010>, 2005.

705 Dayan, U., and Morin, E.: Flash flood – producing rainstorms over the Dead Sea: A  
706 review. *Geological Society of America*, 401(4), 53-62,  
707 [https://doi.org/10.1130/2006.2401\(04\)](https://doi.org/10.1130/2006.2401(04)) , 2006.

708 Dayan, U., and Sharon, D.: Meteorological parameters for discriminating between  
709 widespread and spotty storms in the Negev. *Israel Journal of Earth Sciences*,  
710 29(4), 253-256, 1980.

711 Dayan, U., Ziv, B., Margalit, A., Morin, E., and Sharon, D.: A severe autumn storm over  
712 the middle-east: synoptic and mesoscale convection analysis. *Theoretical and*  
713 *Applied Climatology*, 69(1-2), 103-122, <https://doi.org/10.1007/s007040170038>,  
714 2001.

715 Doms, G., and Baldauf, M.: A Description of the Nonhydrostatic Regional COSMO-  
716 Model. Part I: Dynamics and Numerics. *Deutscher Wetterdienst*, 2015.

717 Doswell, C., and Rasmussen, E.: The Effect of Neglecting the Virtual Temperature  
718 Correction on CAPE Calculations. *Weather and Forecasting*, 9(4), 625-629,  
719 [https://doi.org/10.1175/1520-0434\(1994\)009<0625:TEONTV>2.0.CO;2](https://doi.org/10.1175/1520-0434(1994)009<0625:TEONTV>2.0.CO;2), 1994.

720 FAO/IIASA/ISRIC/ISSCAS/JRC.: *Harmonized World Soil Database (version 1.2)*. FAO,  
721 Rome, Italy and IIASA, Laxenburg, Austria, (accessed 01.02.2017) , 2009.

722 Fosser, G., Khodayar, S., and Berg, P., 2014: Benefit of convection permitting climate

723 model simulations in the representation of convective precipitation, *Clim. Dyn.*,  
724 44(1– 2), 45– 60.

725 Gavrieli, I., Bein, A., and Oren, A., 2005: The expected impact of the “Peace Conduit”  
726 project (the Red Sea - Dead Sea pipeline) on the Dead Sea. *Mitigation and*  
727 *Adaptation Strategies for Global Change*, 10(4), 759-777,  
728 <https://doi.org/10.1007/s11027-005-5144-z>.

729 European Commission, Joint Research Centre, 2003: Global Land Cover 2000  
730 database, (accessed 01.02.2017).

731 GLOBE National Geophysical Data Center, 1999: Global Land One-kilometer Base  
732 Elevation (GLOBE) v.1. Hastings, D. and P.K. Dunbar. National Geophysical  
733 Data Center, NOAA, (accessed 01.02.2017).

734 Greenbaum, N., Ben-Zvi, A., Haviv, I., and Enzel, Y., 2006: The hydrology and  
735 paleohydrology of the Dead Sea tributaries. *Geological Society of America*,  
736 401(4), 63-93, [https://doi.org/10.1130/2006.2401\(05\)](https://doi.org/10.1130/2006.2401(05)).

737 Haylock, M.R., Hofstra, N., Klein Tank, A.M.G., Klok, E.J., Jones, P.D. and New, M.  
738 2008, A European daily high-resolution gridded dataset of surface temperature and  
739 precipitation. *Journal of Geophysical Research: Atmospheres*, 113, D20119.  
740 <https://doi.org/10.1029/2008JD10201>.

741

742 Hochman, A., Mercogliano, P., Alpert, P., Saaroni, H. and Buchignani, E., 2018. High-  
743 resolution projection of climate change and extremity over Israel using COSMO-CLM.  
744 *International Journal of Climatology*, 38(14), pp.5095-5106.

745

746 Houze, R., 2012: Orographic effects on precipitating clouds. *Reviews of Geophysics*,  
747 50(1), <https://doi.org/10.1029/2011RG000365>.

748 Kalthoff, N., Horlacher, V., Corsmeier, U., Volz-Thomas, A., Kolahgar, B., Geiß, H.,  
749 Möllmann-Coers, M., and Knaps, A. 2000: Influence of valley winds on transport  
750 and dispersion of airborne pollutants in the Freiburg-Schauinsland area, *J.*  
751 *Geophys. Res. Atmos*, 105, 1585–1597, <https://doi.org/10.1029/1999jd900999>.

752

753 Khodayar, S., Kalthoff, N., and Schaedler, G., 2013: The impact of soil moisture  
754 variability on seasonal convective precipitation simulations. Part I: validation,  
755 feedbacks, and realistic initialisation. *Meteorologische Zeitschrift*, 22(4), 489-505,  
756 <https://doi.org/10.1127/0941-2948/2013/0403>.

757 Kunin, P., Alpert, P. and Rostkier-Edelstein, D., 2019. Investigation of sea-  
758 breeze/foehn in the Dead Sea valley employing high resolution WRF and observations.  
759 Atmospheric Research.  
760

761 Lensky, N. and Dente, E., 2015. The hydrological processes driving the accelerated  
762 Dead Sea level decline in the past decades. Geological Survey of Israel Report.  
763

764 Llasat, M., and Coauthors, 2010: High-impact floods and flash floods in Mediterranean  
765 countries: the FLASH preliminary database. *Advances in Geosciences*, 23, 47-  
766 55, <https://doi.org/10.5194/adgeo-23-47-2010>.

767 Metzger, J., Nied, M., Corsmeier, U., Kleffmann, J., and Kottmeier, C., 2017: Dead Sea  
768 evaporation by eddy covariance measurements versus aerodynamic, energy  
769 budget, Priestley-Taylor, and Penman estimates. *Hydrology and Earth System  
770 Sciences Discussions*, 22(2), 1135-1155, [https://doi.org/10.5194/hess-2017-  
771 187](https://doi.org/10.5194/hess-2017-187).

772 Miglietta MM, Conte D, Mannarini G, Lacorata G, Rotunno R. 2011. Numerical analysis  
773 of a Mediterranean 'hurricane' over south-eastern Italy: sensitivity experiments to sea  
774 surface temperature. *Atmos. Res.* **101**: 412–426.  
775

776 Moncrieff, M., and Miller, M., 1976: The dynamics and simulation of tropical  
777 cumulonimbus and squall lines. *Quarterly Journal of the Royal Meteorological  
778 Society*, 102(432), 373-394, <https://doi.org/10.1002/qj.49710243208>, 2014.

779 Naor, R., Potchter, O., Shafir, H., and Alpert, P.: An observational study of the  
780 summer Mediterranean Sea breeze front penetration into the complex  
781 topography of the Jordan Rift Valley, *Theor. Appl. Climatol.*, 127, 275–284,  
782 <https://doi.org/10.1007/s00704-015-1635-3>, 2017.

783 Prein, A., Gobiet, A., Suklitsch, M., Truhetz, H., Awan, N., Keuler, K., and Georgievski,  
784 G. : Added value of convection permitting seasonal simulations, *Clim.  
785 Dyn.*, 41(9– 10), 2655– 2677, 2013.

786 Ritter, B., and J.-F. Geleyn, 1992. A comprehensive radiation scheme for numerical  
787 weather prediction models with potential applications in climate simulations. *Mon. Wea.  
788 Rev.*, 120, 303–325.



789 Rostkier-Edelstein, D., Liu, Y., Wu, W., Kunin, P., Givati, A. and Ge, M., 2014. Towards  
790 a high-resolution climatology of seasonal precipitation over Israel. *International*  
791 *Journal of Climatology*, 34(6), pp.1964-1979.  
792

793 Schaedler, G., and Sasse, R.: Analysis of the connection between precipitation and  
794 synoptic scale processes in the Eastern Mediterranean using self-organizing maps.  
795 *Meteorologische Zeitschrift*, 15(3), 273-278, [https://doi.org/10.1127/0941-](https://doi.org/10.1127/0941-2948/2006/0105)  
796 [2948/2006/0105](https://doi.org/10.1127/0941-2948/2006/0105), 2006.

797 Shafir, H., and Alpert, P.: Regional and local climatic effects on the Dead-Sea  
798 evaporation. *Climatic Change*, 105(3-4), 455-468,  
799 <https://doi.org/10.1007/s10584-010-9892-8>, 2011.

800 Sharon, D., and Kutiel, H.: The distribution of rainfall intensity in Israel, its regional and  
801 seasonal variations and its climatological evaluation. *International Journal of*  
802 *Climatology*, 6(3), 277-291, <https://doi.org/10.1002/joc.3370060304>, 1986.

803 Smiatek, G., Kunstmann, H., and Heckl, A.: High-resolution climate change simulations  
804 for the Jordan River area. *Journal of Geophysical Research*, 116(D16),  
805 <https://doi.org/10.1029/2010JD015313>, 2011.

806 Stanhill, G.: Changes in the rate of evaporation from the dead sea. *International*  
807 *Journal of Climatology*, 14(4), 465-471,  
808 <https://doi.org/10.1002/joc.3370140409>,1994.

809 Vicente-Serrano, S., Beguería, S., López-Moreno, J.: A Multiscalar Drought Index  
810 Sensitive to Global Warming: The Standardized Precipitation  
811 Evapotranspiration Index. *J. Climate*, 23(7), 1696-1718,  
812 <https://doi.org/10.1175/2009JCLI2909.1>, 2010.

813 Vüllers, J., Mayr, G. J., Corsmeier, U., and Kottmeier, C.: Characteristics and  
814 evolution of diurnal foehn events in the Dead Sea valley. *Atmos. Chem. Phys.*,  
815 18, 18169-18186, <https://doi.org/10.5194/acp-18-18169-2018>, 20, 2018.  
816

817 Wernli H, Paulat M, Hagen M, Frei C. SAL – a novel quality measure for the  
818 verification of quantitative precipitation forecasts. *Mon. Weather Rev.* 136: 4470–  
819 4487, 2008.  
820

821 Yatagai, A., Alpert, P. and Xie, P. (2008) Development of a daily gridded precipitation  
822 data set for the Middle East. *Advances in Geosciences*, 12, 1–6.

823

824 Yatagai, A., Kamiguchi, K., Arakawa, O., Hamada, A., Yasutomi, N. and Kitoh, A.,  
825 2012: APHRODITE: constructing a long-term daily gridded precipitation dataset for  
826 Asia based on a dense network of rain gauges. *Bulletin of the American Meteorological*  
827 *Society*, 93, 1401–1415.

828

829

830

831

832

833

834

835

836

837

838

839

840

841

842

843

844

845

846

847

848 **Tables**

	PREC diffmn	REF PMX	SEN PMX	PREC relative diff [%]	Synoptic Situation	REF CAPEmx	SEN CAPEmx	REF KOmn	SEN KOmn	Localised/ Widespread (Subarea affected)
08.12.2004	0,10	30,09	31,31	2,76	ARST	1	1	4,85	4,85	W (A1, A2)
13.01.2006	-0,11	45,64	54,64	-4,26	Cyprus Low	239	225	6,57	6,54	L/W (A1, A3)
16.04.2006	0,11	57,41	56,09	4,89	Syrian Low	43	47	1,97	1,94	L (A1, A4)
10.04.2007	0,29	42,61	70,20	30,78	Cyprus Low	686	679	-4,77	-4,70	L (A2, A4)
13.04.2007	0,12	134,3 6	127,7 9	1,62	Cyprus Low	573	576	-1,95	-1,92	L (A1, A2, A3, A4)
12.05.2007	-0,16	41,82	47,90	-8,24	Syrian Low	436	81	-5,30	-5,29	L (A1, A2)
27.01.2008	-0,14	23,11	17,24	-17,25	Syrian Low	7	7	5,12	5,12	W (A1, A3)
25.10.2008	-0,23	139,0 1	125,7 3	-16,52	ARST	1274	1361	-5,50	-4,08	L (A3)
13.11.2008	0,30	40,83	45,55	25,68	ARST	25	7	1,37	1,38	L (A2, A4)
14.05.2009	-0,39	59,28	68,84	-8,49	Syrian Low	433	429	-3,90	-3,91	L (A1, A2, A3, A4)
15.05.2009	0,20	49,23	42,28	13,50	Syrian Low	208	203	-2,30	-2,36	L (A1, A2, A3)
31.10.2009	-0,19	166,2 1	111,7 9	-7,65	Cyprus Low	435	445	-5,03	-4,46	L (A1, A2)
15.01.2011	0,11	73,02	72,03	3,74	Syrian Low	49	37	7,82	7,83	L/W (A1, A4)
28.05.2011	-0,24	44,51	32,73	-14,33	Cyprus Low	158	170	-10,27	-10,26	W (A2)
14.11.2011	-0,11	42,65	9,34	-65,90	Cyprus Low	2	0	-7,14	-7,12	L (A1, A2)
17.11.2011	0,11	90,07	93,04	4,76	Cyprus Low	386	304	-9,14	-9,16	L (A1)
18.11.2011	-0,11	28,68	34,69	-8,67	Cyprus Low	356	378	-8,61	-8,65	L (A1)
19.11.2011	0,03	58,11	12,36	4,09	Cyprus Low	133	81	-7,60	-7,46	L (A2, A4)
22.10.2012	0,20	29,88	41,64	51,21	ARST	2068	2097	-5,83	-5,59	L (A1, A2)
09.11.2012	-0,11	27,20	22,56	-18,29	Cyprus Low	218	215	3,97	3,98	W (A1)
23.11.2012	-0,21	155,7 7	117,8 1	-10,17	ARST	189	286	-2,18	-1,95	L (A1, A2, A3)
25.11.2012	-0,11	41,48	54,33	-7,87	ARST	354	332	4,19	4,37	L (A3, A4)

849

850

851 **Table 1:** Classification of heavy precipitation cases in the decadal simulation covering  
852 the period 2004 to 2013. The areal-mean (study area, Figure 1) difference (PREC<sub>diffmn</sub>)  
853 and maximum grid precipitation in the reference (REF<sub>PMX</sub>) and sensitivity (SEN<sub>PMX</sub>)  
854 realizations, the precipitation relative difference in %, the synoptic situation, and the  
855 stability conditions illustrated by maximum grid point CAPE (CAPEmx) and minimum  
856 grid point KO-index (KOmn) are summarized. Additionally, the nature of the  
857 precipitation, localized (L) or widespread (W) and the main subarea affected (following  
858 division in Figure 1; A1, A2, A3, A4) are listed.

859

860

861

862

863

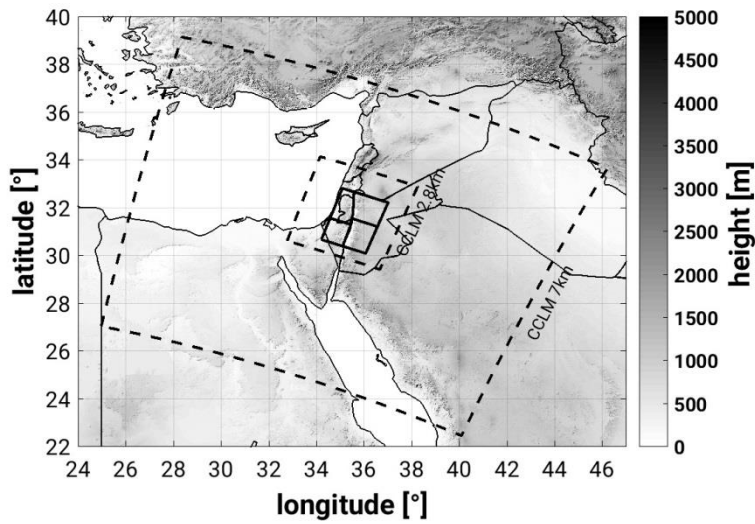
864

865

866

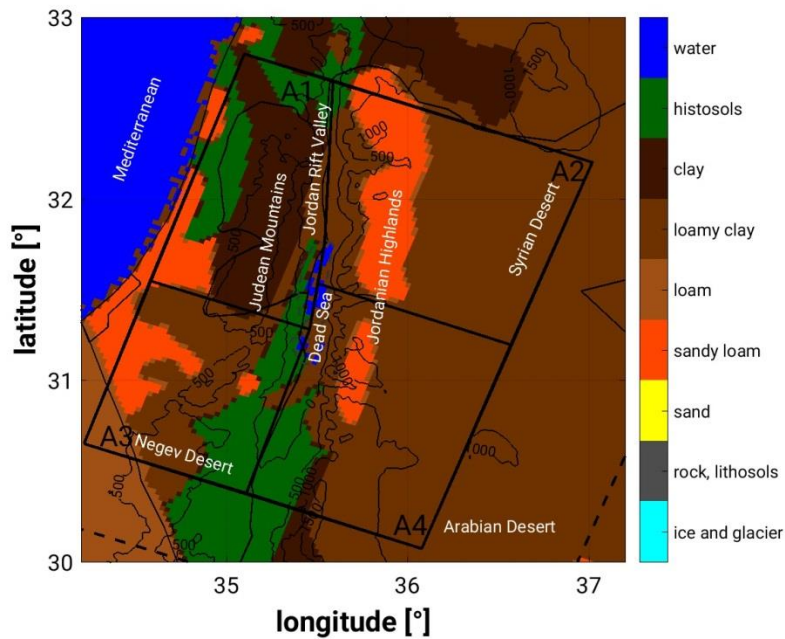
867 **Figures**

868 (a)



869

870 (b)



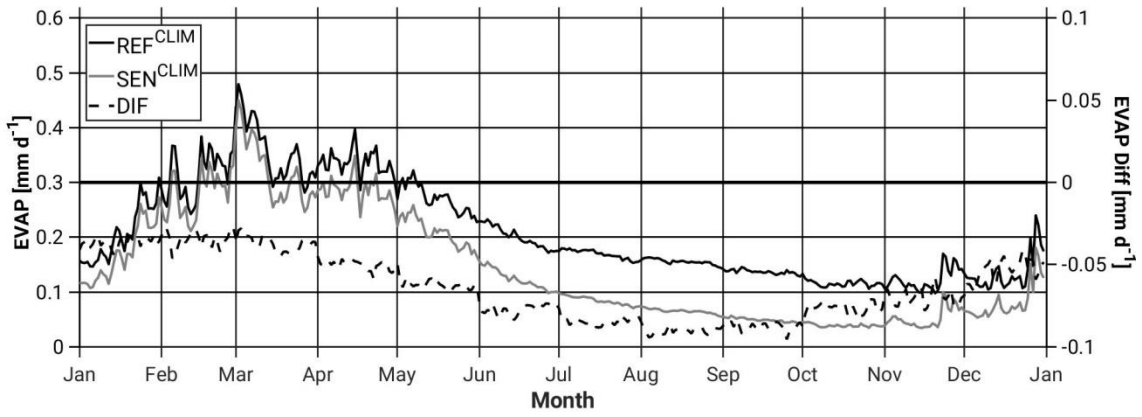
871

872

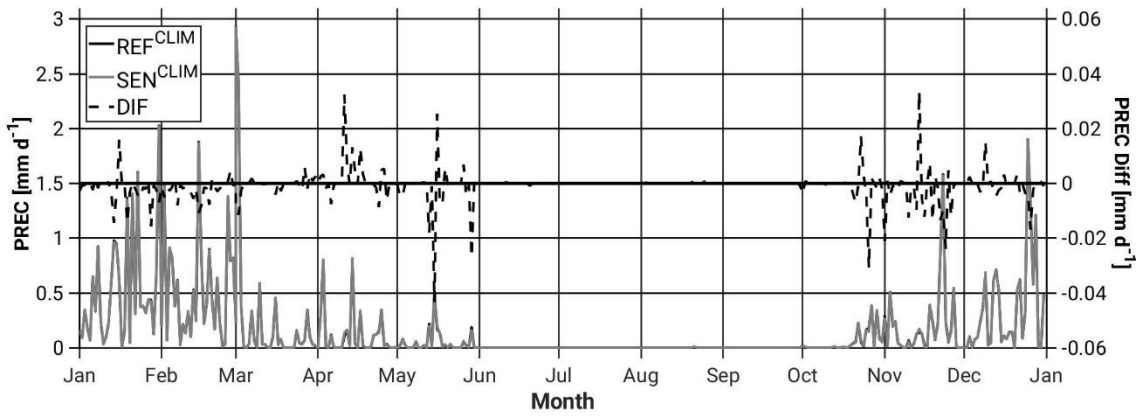
873 Figure 1: (a) Topography (m above msl), simulation domains (dashed lines, CCLM7km  
874 and CCLM2.8km) and study area (bold line). (b) Model soil types (colour scale),  
875 topography (black isolines) and study area (black bold line) including the 4 subdomains  
876 to be examined, A1-4 (Area 1-4).

877 (a)

878

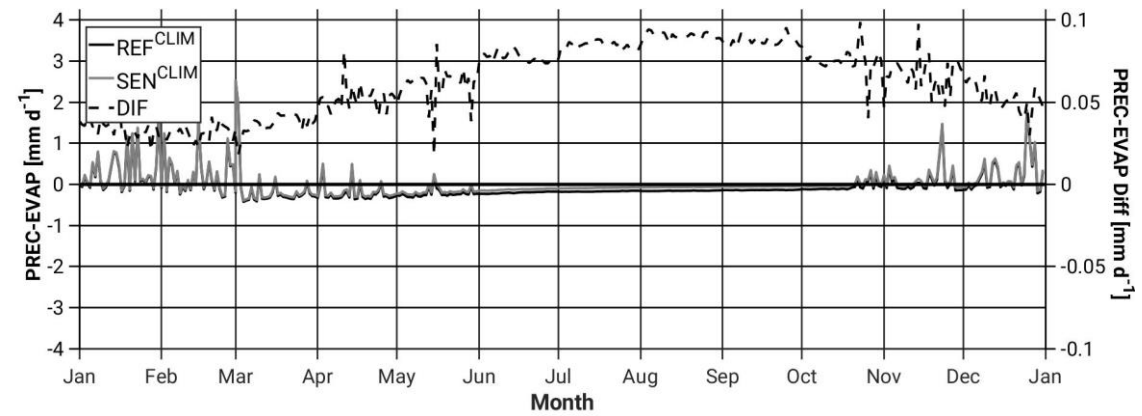


879



880

881



882

883

884

885

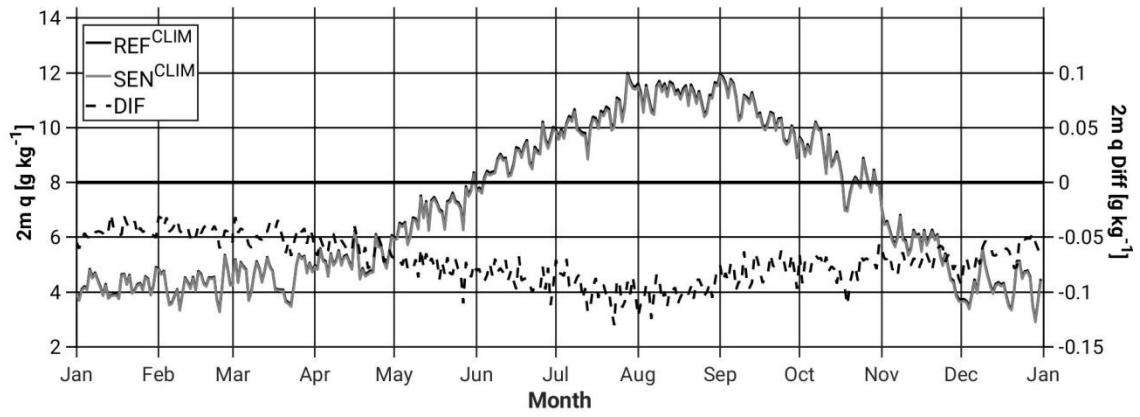
886

887

888

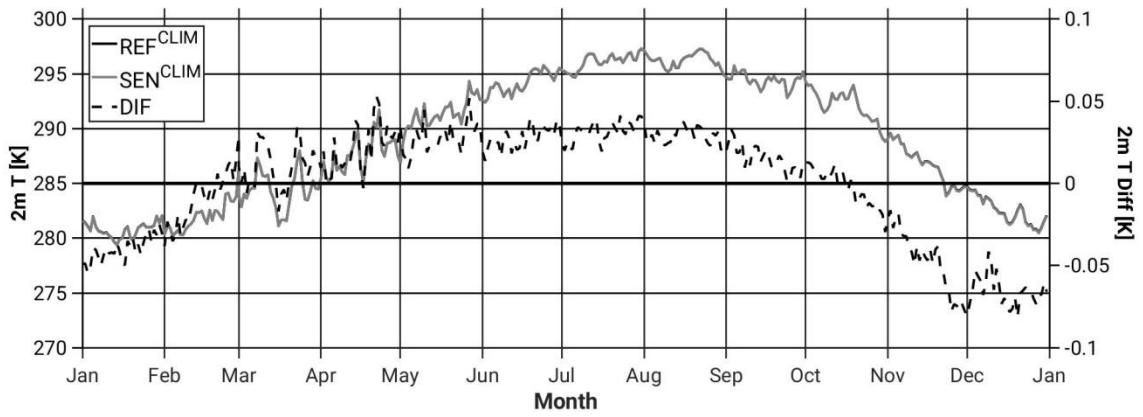
889

890 (b)



891

892



893

894

895

896

897

898

899

900

901

902

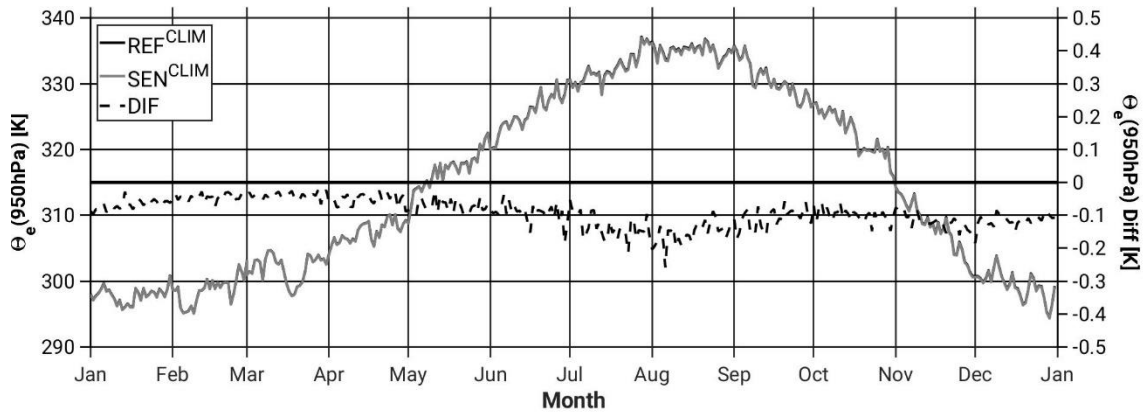
903

904

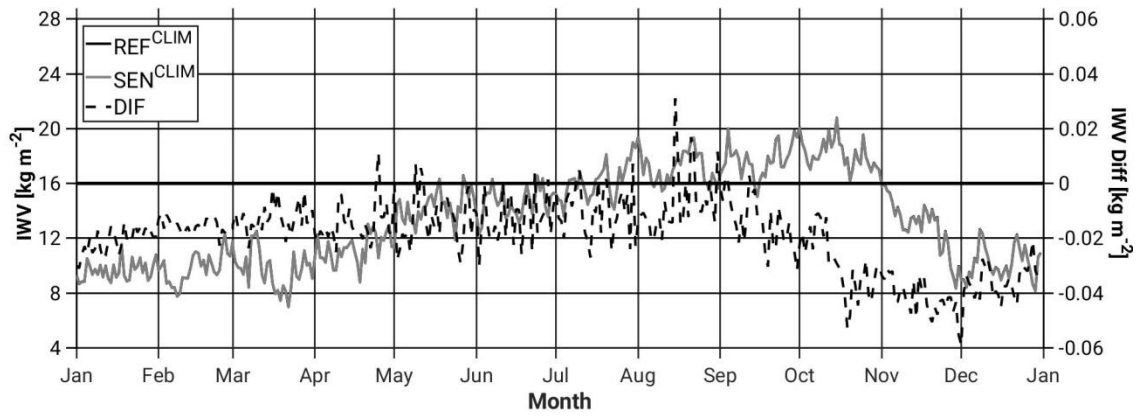
905

906 (c)

907



908



909

910

911

912

913

914

915

916

917

918

919

920

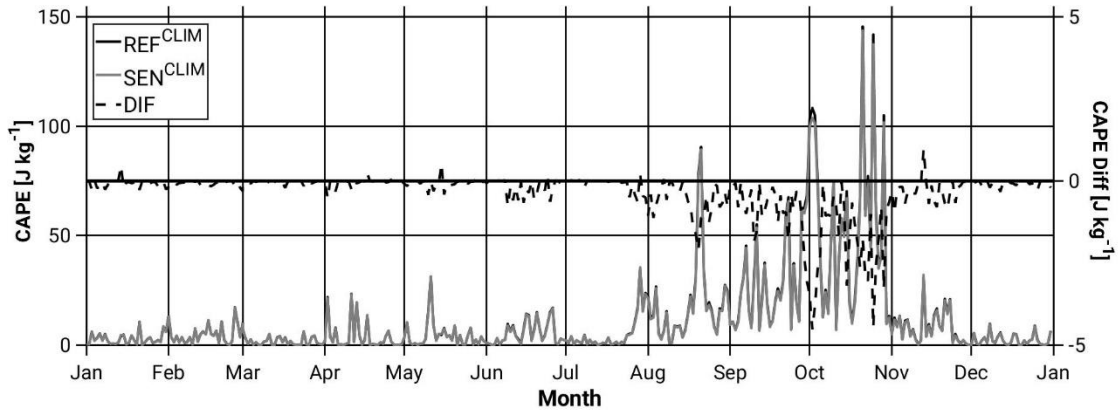
921

922

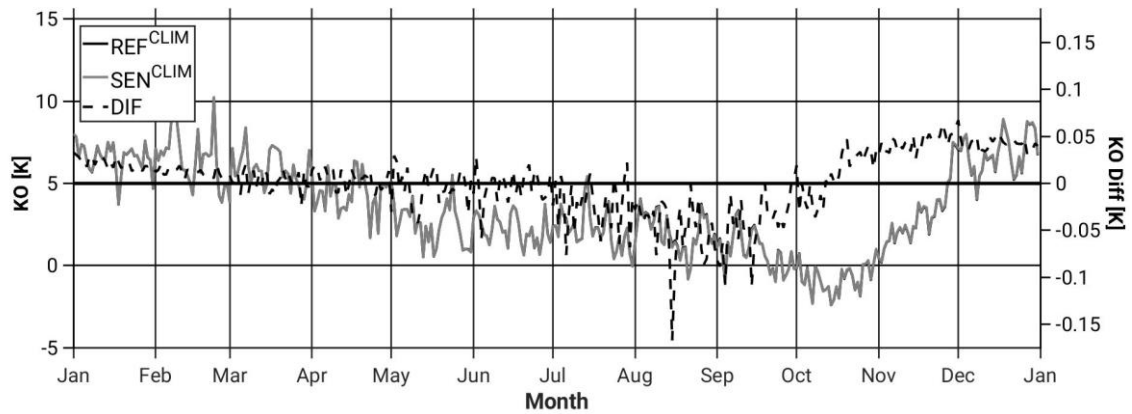
923

924 (d)

925



926



927

928

929

930 Figure 2: Annual cycle of the area-averaged daily accumulated (and differences (black  
931 dashed line; SEN-REF)) of (a) evaporation, precipitation, and precipitation minus  
932 evaporation (b) specific humidity and temperature at 2-m, and (c)  $\Theta_e$  below 950 hPa  
933 and IWV, and (d) CAPE and KO-index, from the REF<sup>CLIM</sup> (full black line) and the  
934 SEN<sup>CLIM</sup> (full grey line) simulations. All grid points in the study area (Figure 1) and the  
935 period 2004 to 2013 are considered.

936

937

938

939

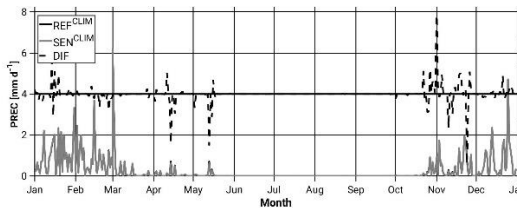
940

941

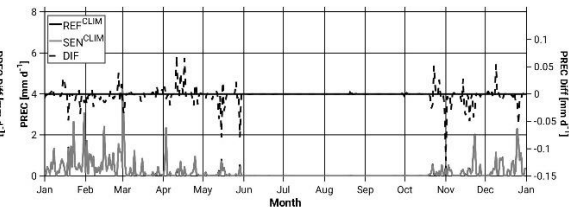
942 (a)



943 Area1 (NW)

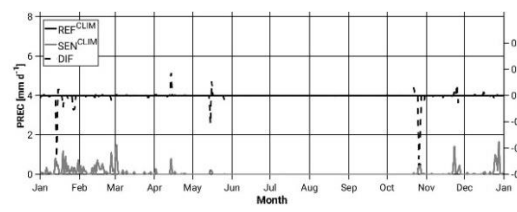


Area2 (NE)

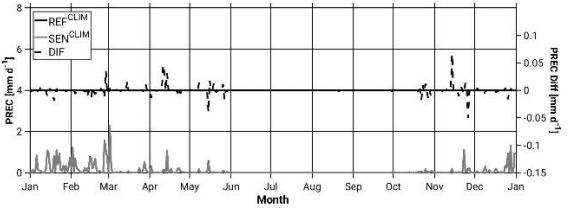


944

945 Area3 (SW)



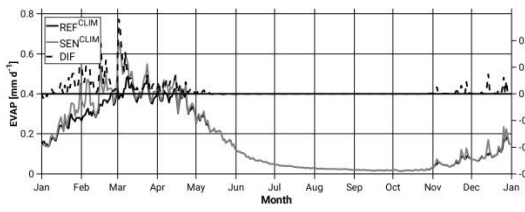
Area4 (SE)



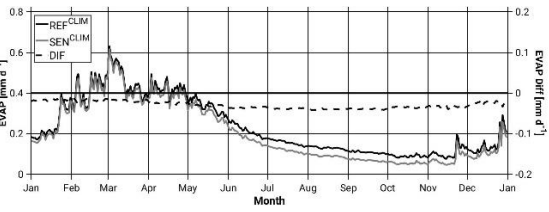
946

947 (b)

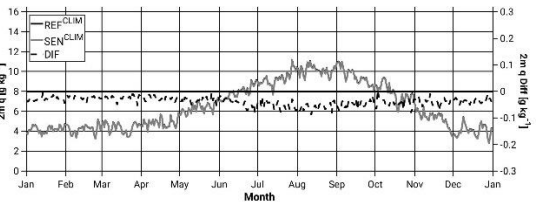
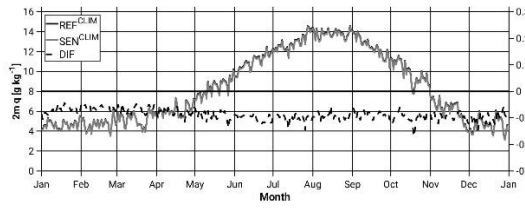
948 Area1 (NW)



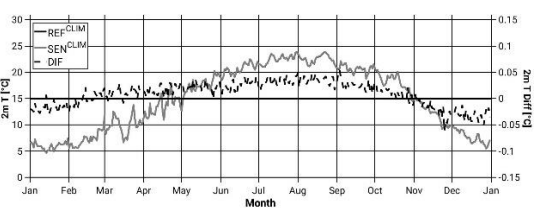
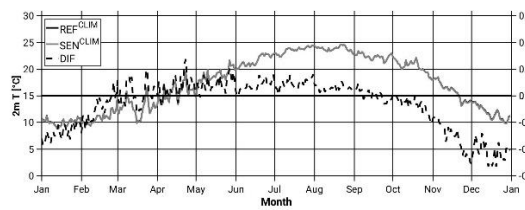
Area2 (NE)



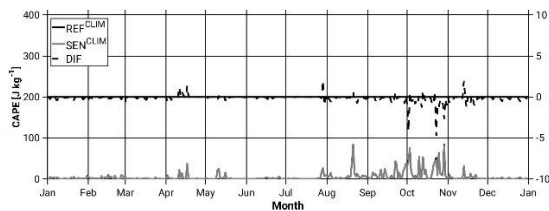
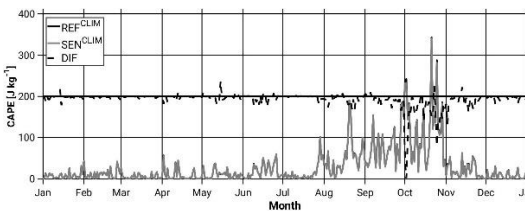
949



950



951



952

953

954

955 Figure 3: Annual cycle of the areal-daily averaged (and differences (black dashed line;  
956 SEN-REF)) of (a) precipitation for areas A1, A2, A3, A4 (see Figure 1b), and (b)  
957 evaporation, specific humidity and temperature at 2-m, and CAPE for areas A1 and A2,  
958 from the REF<sup>CLIM</sup> (full black line) and the SEN<sup>CLIM</sup> (full grey line) simulations. Only land  
959 points in the study area (Figure 1) for evaporation, and all grid points for the rest of  
960 variables and the period 2004 to 2013 are considered.

961

962

963

964

965

966

967

968

969

970

971

972

973

974

975

976

977

978

979

980

981

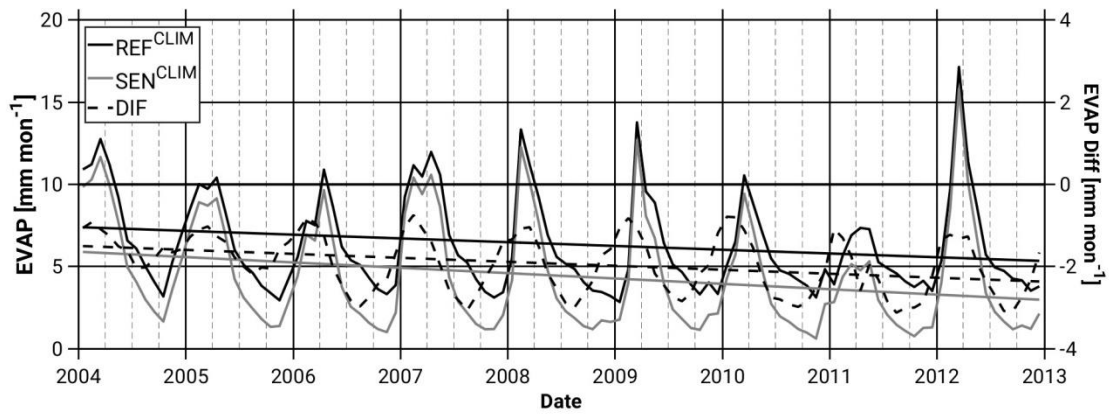
982

983

984

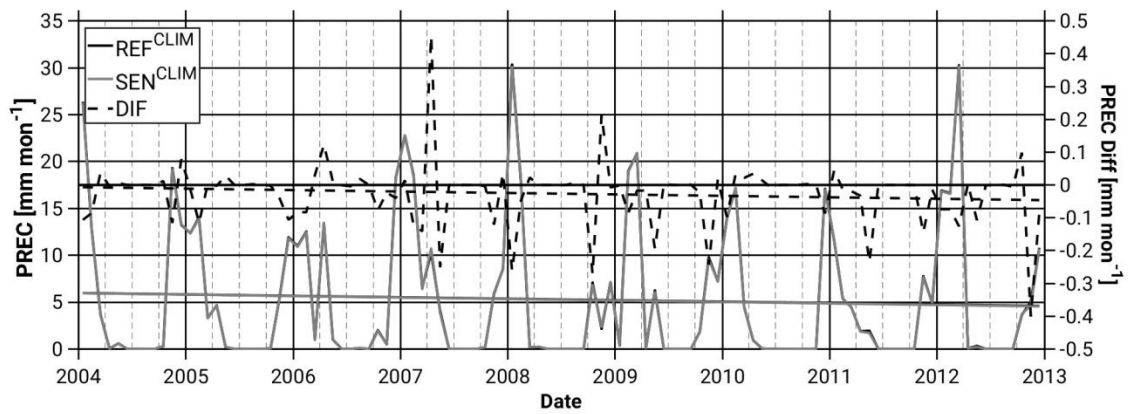
985

986 (a)



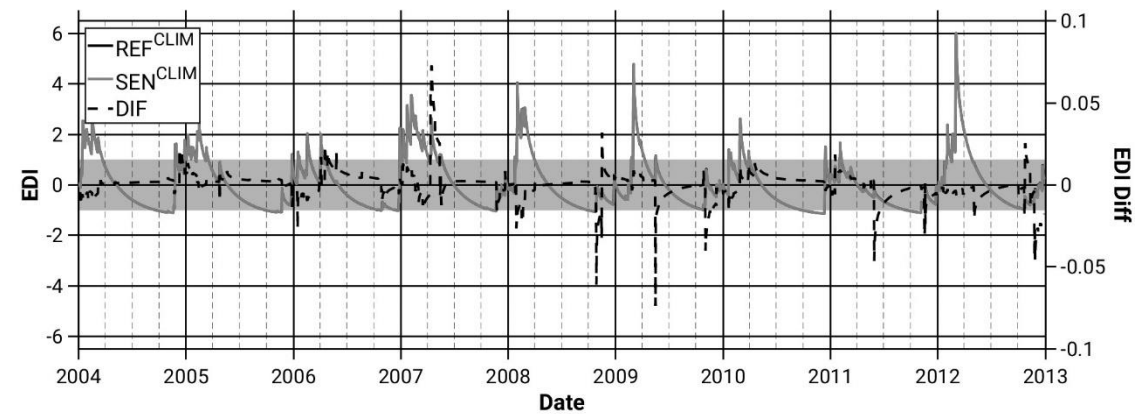
987

988 (b)



989

990 (c)



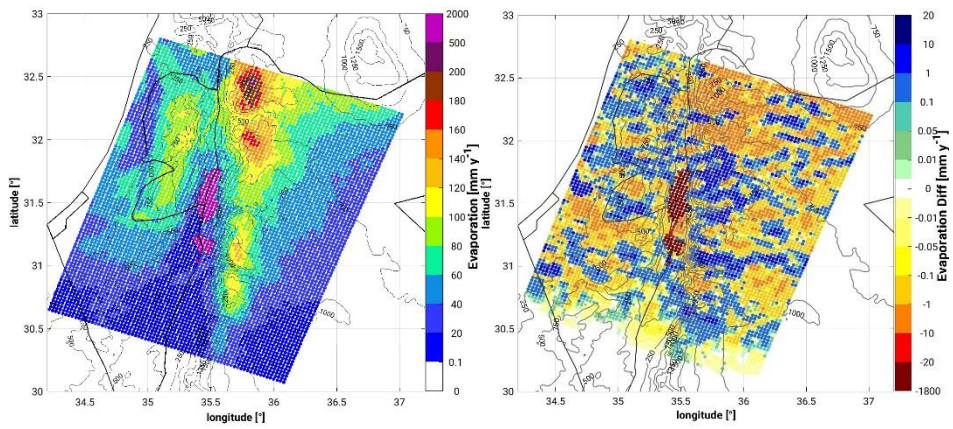
991

992 Figure 4: Temporal evolution of the area-averaged monthly accumulated values of (a)  
993 Evaporation, (b) Precipitation, (c) Effective Drought Index (EDI), from the REF<sup>CLIM</sup> (full  
994 black line) and the SEN<sup>CLIM</sup> (full grey line) simulations and differences depicted with  
995 black dashed lines. The light grey band in (c) indicates the common soil state (-  
996 1 < EDI < +1). All grid points in the study area (Figure 1) and the period 2004 to 2013 are  
997 considered.

998

999

1000 (a)

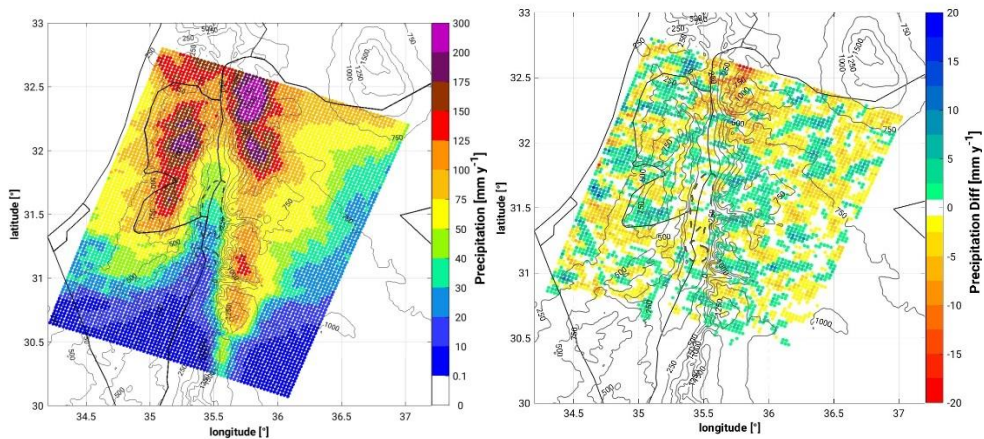


1001

1002

1003

1004 (b)



1005

1006

1007

1008 Figure 5: Spatial distribution of (a) evaporation in the REF<sup>CLIM</sup> simulation (left) and the  
1009 difference between the SEN<sup>CLIM</sup> and the REF<sup>CLIM</sup> simulations (right), and (b)  
1010 precipitation in the REF<sup>CLIM</sup> simulation (left) and the difference between the SEN<sup>CLIM</sup>  
1011 and the REF<sup>CLIM</sup> simulations (right). The period 2004 to 2013 is considered.

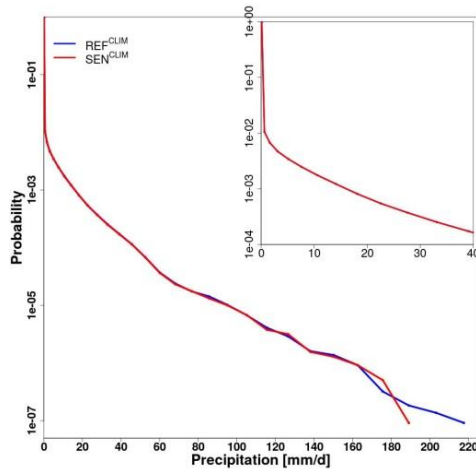
1012

1013

1014

1015

1016 (a)

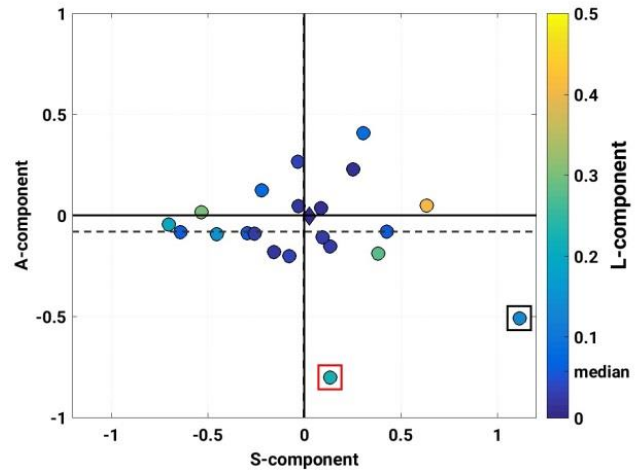


1017

1018

1019

(b)



1020 Figure 6: (a) Probability density function of daily precipitation intensities. All grid points  
1021 in the investigation domain (Figure 1) and the period 2004 to 2013 are considered. (b)  
1022 SAL diagram between  $REF^{CLIM}$  and  $SEN^{CLIM}$  simulations. Every circle corresponds to a  
1023 simulated heavy precipitation event (listed in Table 1). The diamond (close to the zero-  
1024 zero) illustrates the mean of all events. A-component (amplitude), S-component  
1025 (structure), L-component (location). The inner colour indicates the L-component. Boxes  
1026 point out the two events examined in this study, CASE1 and CASE2 (see section 3.2).

1027

1028

1029

1030

1031

1032

1033

1034

1035

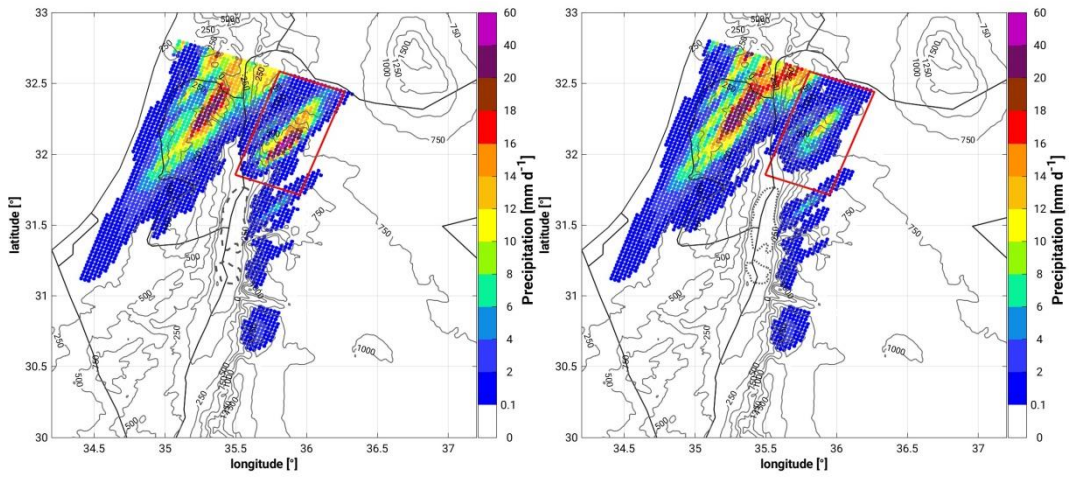
1036

1037

1038

1039

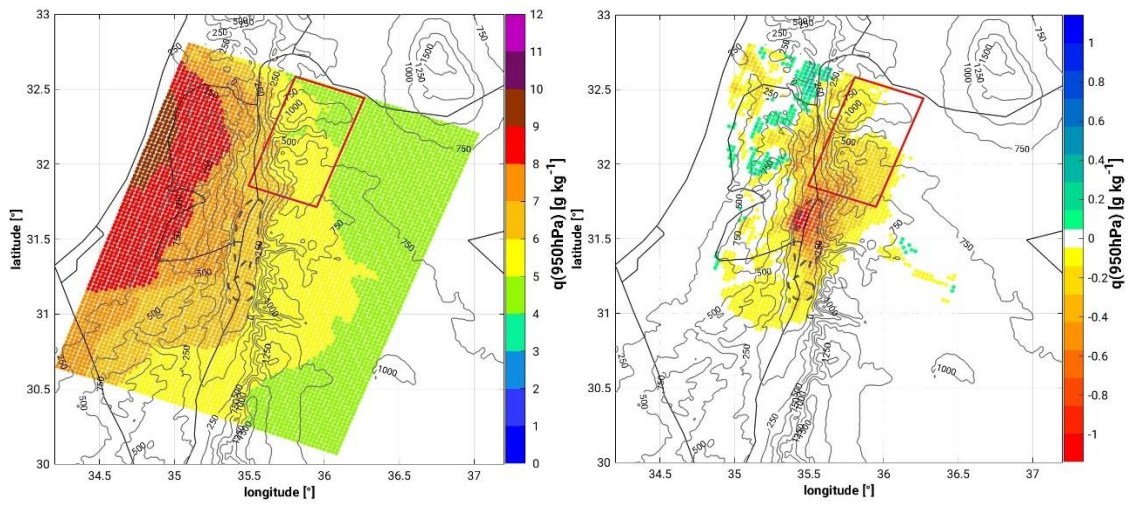
1040 (a)



1041

1042 (b)

1043



1044

1045

1046

1047

1048

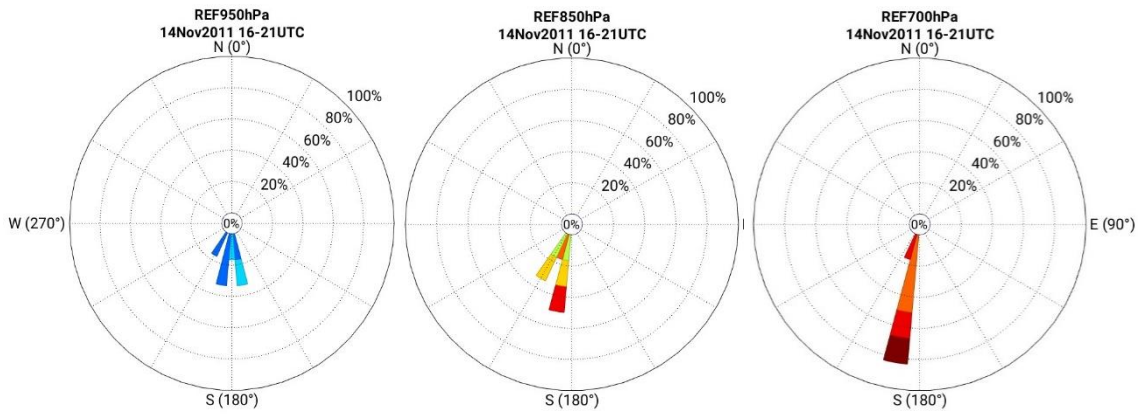
1049

1050

1051

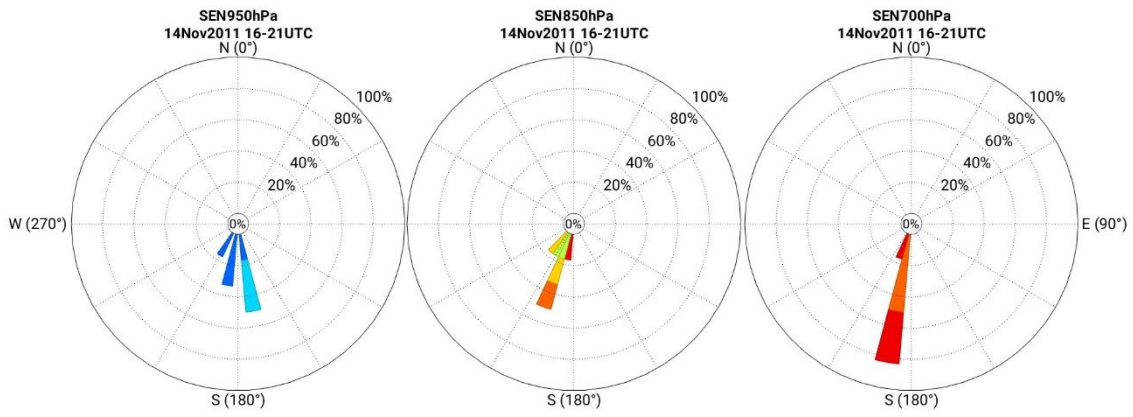
1052

1053 (c)



1054

1055



1056



1057

1058

1059

1060

1061

1062 Figure 7: Spatial distribution of (a) 24-h accumulated precipitation from 14.11 09 UTC  
1063 to 15.11 08 UTC from the REF<sup>14.11</sup> simulation (left) and the SEN<sup>14.11</sup> simulation (right)  
1064 and (b) specific humidity below 950 hPa, from the REF<sup>14.11</sup> simulation (left) and the  
1065 difference between the REF<sup>14.11</sup> and SEN<sup>14.11</sup> simulations, as a mean for the 6-h period  
1066 prior to convection initiation in the target area (14 November 16 UTC to 21 UTC), and  
1067 (c) wind conditions at 700 hPa, 850 hPa, and 950 hPa (no relevant differences with  
1068 respect to the 10-m field) for the same time period. Wind roses are centred at about  
1069 35.82°E-32.07°N in our target area.

1070

1071

1072

1073

1074

1075

1076

1077

1078

1079

1080

1081

1082

1083

1084

1085

1086

1087

1088

1089

1090

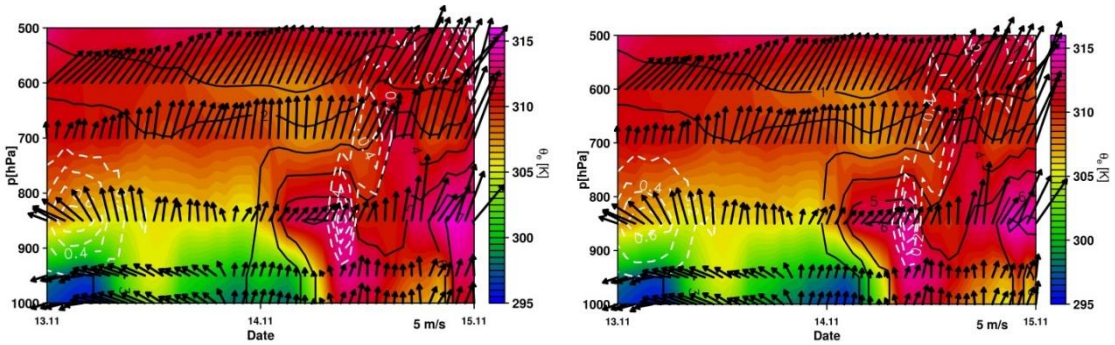
1091

1092



1093

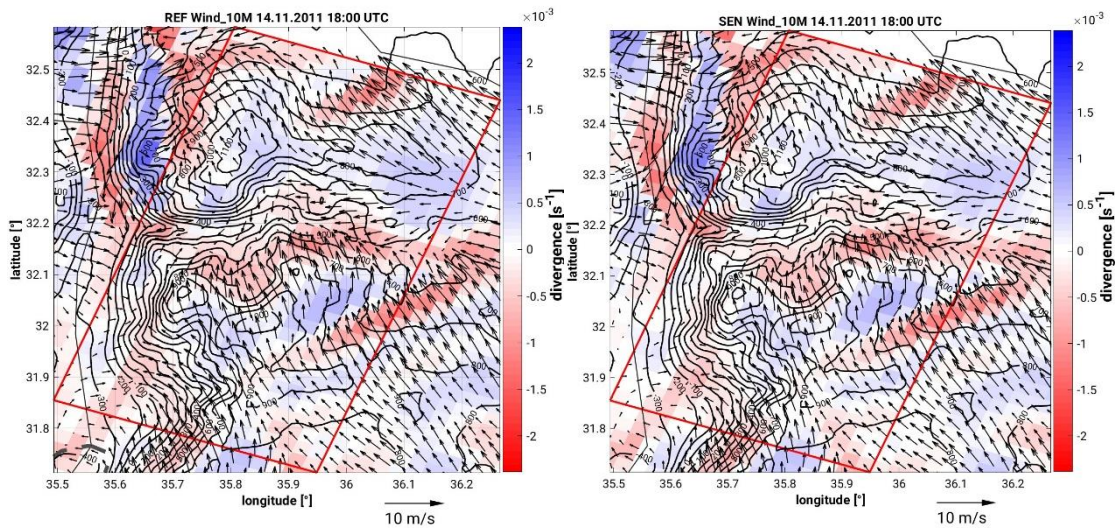
1094 (a)



1095

1096 (b)

1097



1098

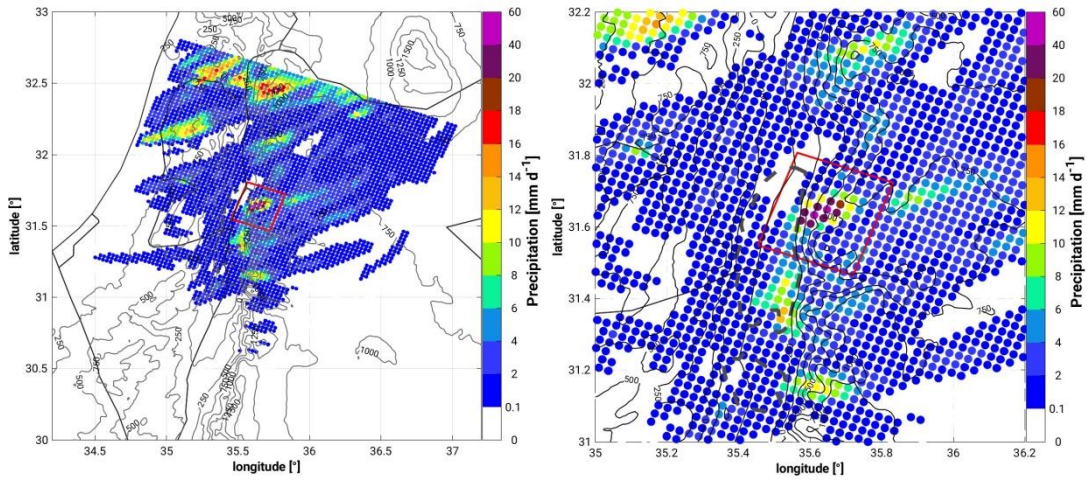
1099

1100 Figure 8: (a) Vertical-temporal cross-section of equivalent potential temperature (colour  
1101 scale; K), specific humidity (black isolines; g/kg), horizontal wind vectors (north-pointing  
1102 upwards, m/s) and vertical velocity (white dashed contours with 0.1 m/s increments) of  
1103 the REF<sup>14.11</sup> (left) and SEN<sup>14.11</sup> (right) simulations, over a representative grid point in the  
1104 sub-study region, 32.05°N 35.79°E. (b) Spatial distribution of 10-m horizontal wind  
1105 (wind vectors; m/s) and corresponding divergence/convergence field (colour scale; s<sup>-1</sup>)  
1106 at 18 UTC on the 14 November 2011 from the REF<sup>14.11</sup> (left) and SEN<sup>14.11</sup> (right)  
1107 simulations.

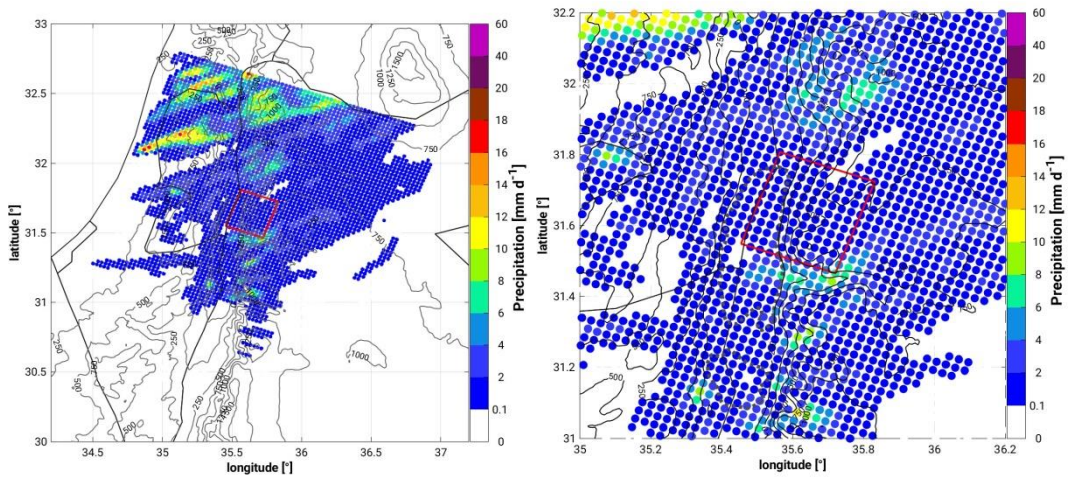
1108

1109

1110



1111  
1112



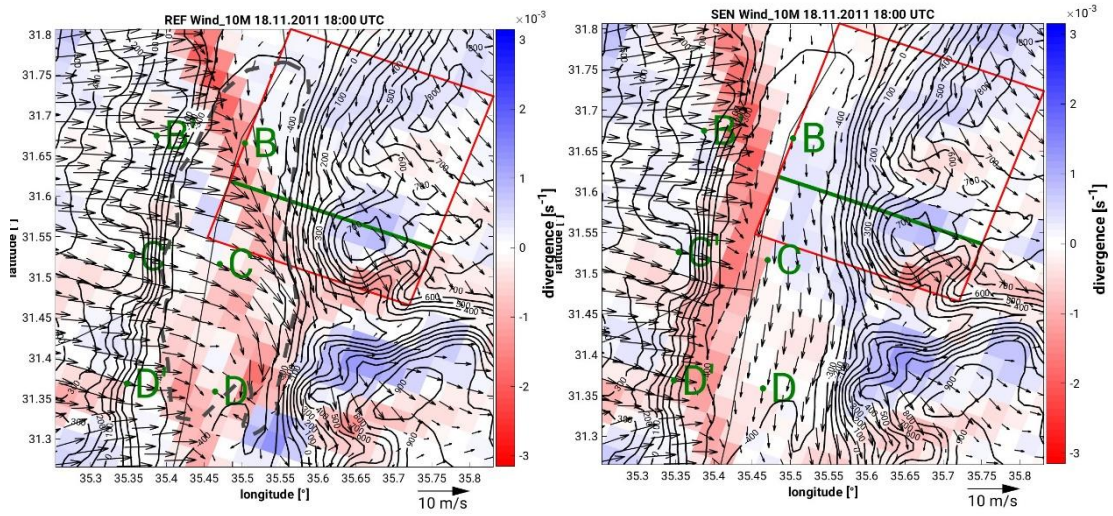
1113  
1114  
1115  
1116

1117 Figure 9: 24-h mean spatial distribution of precipitation from the REF<sup>19.11</sup> simulation  
1118 (top-left; zoom top-right) and the SEN<sup>19.11</sup> simulation (bottom-left; zoom bottom-right)  
1119 for the period 18 November 2011 11 UTC to 19 November 2011 10 UTC.

1120  
1121  
1122  
1123  
1124  
1125  
1126

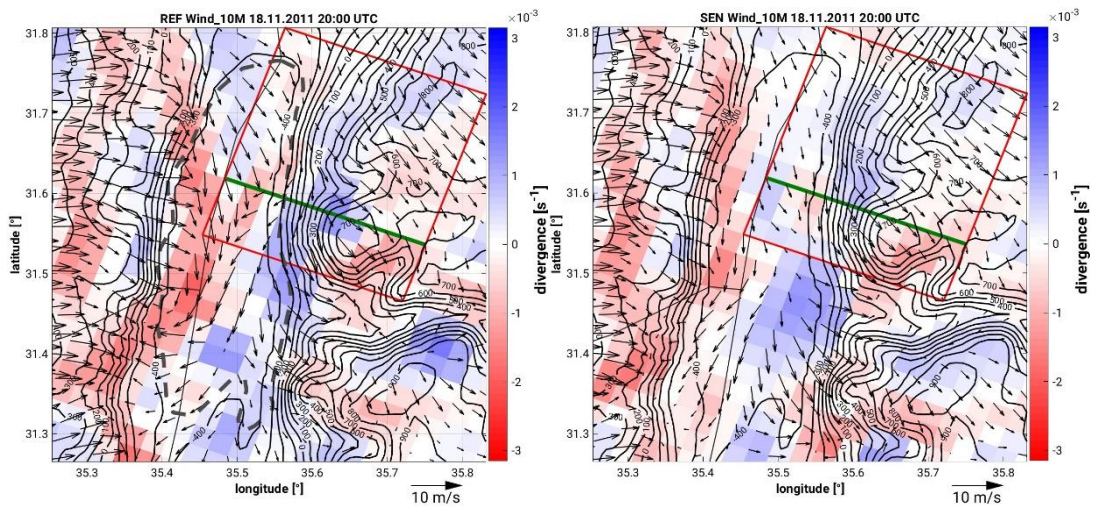
1127

1128 (a)



1129

1130 (b)



1131

1132

1133

1134

1135

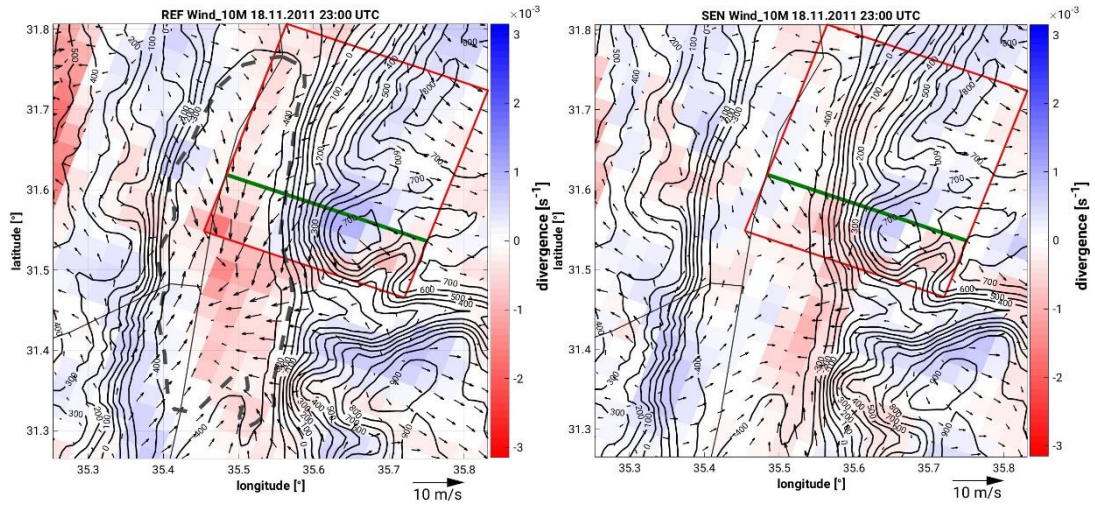
1136

1137

1138

1139

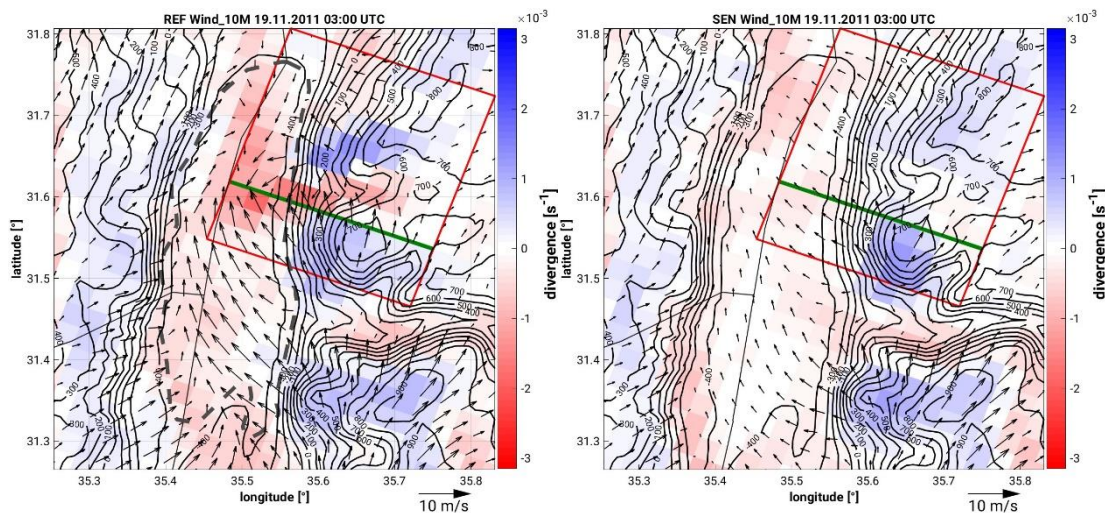
1140 (c)



1141

1142

1143 (d)



1144

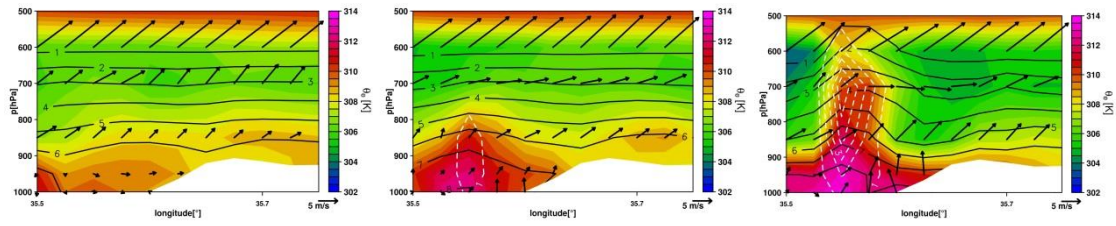
1145

1146 Figure 10: Spatial distribution of 10-m horizontal wind (wind vectors; m/s) and  
1147 corresponding divergence/convergence field (colour scale;  $s^{-1}$ ) at 18 UTC, 20 UTC, 23  
1148 UTC on the 19 November, and 03 UTC on the 20 November 2011 from the REF<sup>19,11</sup>  
1149 (left) and SEN<sup>19,11</sup> (right) simulations. The topography is indicated by the black full  
1150 isolines. The transects (B-C-D and B'-C'-D') corresponding to the locations in which  
1151 temperature comparisons are made are indicated in Figure 10a. The green line  
1152 indicates the position of the vertical cross-section in Figure 11.

1153

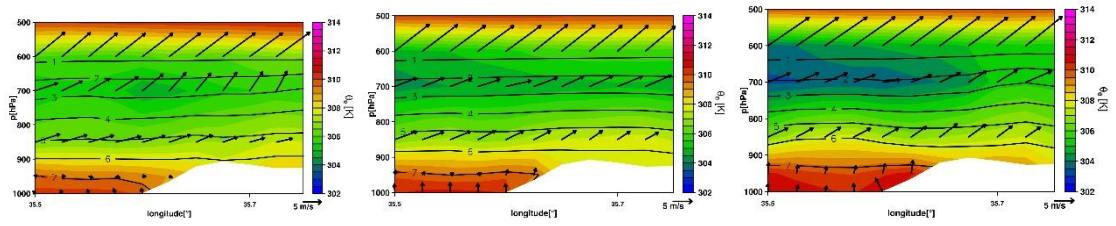
1154

1155



1156

1157



1158

1159

1160

1161 Figure 11: Vertical cross-section of equivalent potential temperature (colour scale; K),  
1162 specific humidity (black isolines; g/kg), horizontal wind vectors (north-pointing upwards,  
1163 m/s) and vertical velocity (white dashed contours with 1 m/s increments) of the REF<sup>19,11</sup>  
1164 (top) and SEN<sup>19,11</sup> (bottom) simulations at 01 UTC (left), 02 UTC (middle) and 03 UTC  
1165 (right). The location of the cross-section is indicated in Figure 10.

1166

1167

1168

1169

1170

1171

1172

1173

1174

1175

1176